Article

Synthesis of a Novel Photocatalyst Based on Silicotitanate Nanoparticles for the Removal of Some Organic Matter from Polluted Water

Amr A. Sayed Alahl [1] , Hesham A. Ezzeldin [2], Abdullah A. Al-Kahtani [3], Sadanand Pandey [4,*] and Yousra H. Kotp [2]

1 Renewable Energy Department, Desert Research Center, Cairo 11753, Egypt
2 Hydrogeochemistry Department, Desert Research Center, Cairo 11753, Egypt
3 Department of Chemistry, College of Science, King Saud University, P.O. Box 2455, Riyadh 11451, Saudi Arabia
4 Department of Chemistry, College of Natural Sciences, Yeungnam University, Gyeongsan 38541, Gyeongbuk, Republic of Korea
* Correspondence: sadanand.au@gmail.com or spandey@ynu.ac.kr

Abstract: The use of waste from various agricultural sectors has recently drawn increased interest from the scientific, technological, ecological, economic, and social fields. As such, in this study, a novel production of an affordable and environmentally friendly photocatalyst of silicotitanate (S1, S2, and S3) made from silica solution (extracted from rice husk ash) and various molar ratios of titanium (IV) 2-ethylhexyl-oxide is reported. Following that, chitosan/silicotitanate (CHMix) nanocomposite material was created through a crosslinking reaction between chitosan and fabricated silicotitanate (S2). Fourier transform infrared spectroscopy (FTIR), X-ray diffraction (XRD), scanning electron microscopy (SEM-EDX), as well as N_2 adsorption-desorption isotherm and zeta potential measurements were used to characterize each of the fabricated samples. Additionally, in comparison to neat chitosan, the newly fabricated material's (CHMix) photocatalytic reactivity was investigated using two synthetic anionic dyes, reactive blue and Congo red, with decolorization rates of up to 95.76% and 99.9%, respectively. The decolorization results showed that CHMix is the most efficient photocatalyst for the degradation of reactive blue and Congo red. Reactive blue and Congo red's molecular structures were almost completely broken when equilibrium was reached using sunlight, and the decolorization rate for both dyes was close to 100%. As a result, the combination of chitosan and silicotitanate, or CHMix, has an effective photocatalytic capability for dye degradation in both natural and concentrated sunlight.

Keywords: solar photocatalytic degradation; chitosan/silicotitanate; nanoparticle; synthetic dyes; reactive blue; Congo red

1. Introduction

Over the past ten years, there has been a significant increase in research on how to effectively combine renewable solar radiation with improved photocatalytic performance to manage freshwater scarcity and the energy crisis. Recent research has suggested that solar energy combined with water evaporation, photocatalytic degradation, sterilization, and hydrogen production offers promising opportunities to the fields of energy production and clean water [1–5]. A wide range of photocatalysis technologies have been applied, boosted by the advancements of functional solar-powered materials that have been thoughtfully designed. Solar photocatalysis is one of these processes that has attracted industrial interest as a viable method for reducing the negative environmental effects of water pollution [6,7]. Diverse photocatalytic processes have been suggested at a pilot scale for the degradation and mineralization of water contaminants such as pesticides, herbicides, dyes, emerging

pollutants, phenols, and halogenated compounds. These processes use solar energy and commercial catalysts [8–11].

The coupling of solar-driven photocatalysts is crucial in order to realize the photocatalysis effect along with solar-driven devices. Numerous functional materials with excellent photo-conversion properties have recently surfaced in the field of photocatalysts for water treatment, including frequently used Ti-based oxides [12–15], metal nanoparticles [16,17], perovskites [18,19], W-based oxides [20–27], and other semiconductors [28–31]. These photocatalysts have attracted a lot of interest because of their wide solar spectrum absorption, significant specific surface area, customized electrical property, and stability. This interest has led researchers to investigate how the photothermal effect can be used to improve the kinetic rates of redox reactions and charge separation efficiency. There have been a lot more articles published recently about photothermal catalysis and solar-driven evaporation. Recently, various inorganic semiconductor nanomaterials, including ZnO, ZnS, CdS, SiO_2, TiO_2, Fe_2O_3, Al_2O_3, and ZrO_2, have been shown to be useful as photo catalysts [32,33]. In addition, they are thought to be safe, biologically inert, chemically stable, and insoluble in water. In particular, one of the key benefits is the cost-effectiveness of TiO_2; it is the most commonly used because of its ability to degrade dye molecules, as well as its non-toxicity, large surface area, and stability in both acidic and basic media [32–35].

Regretfully, TiO_2 cannot be activated by visible light. Due to its wide band gap (3.2 eV) and the low quantum yield of catalysts brought on by the quick recombination of photo-generated electron (e) hole (h^+) pairs, TiO_2 is also insufficient for photocatalytic activities [36]. However, dye adsorption in the dark was found to be lower and photocatalytic activity for CdS/TiO_2 was higher comparedtoTiO_2 [36,37]. Different approaches are used to progress the visible light responsiveness and decrease the charge recombination in pure TiO_2. Doping is one of the many modification methods that can readily change the electronic structure and create new energy levels without altering the primary crystal structure [38–40]; in particular, doping TiO_2 with noble metals (Pt, Ag, and Au), along with non-metals (S, N, C, and P) [38]. Some factors, such as impurities, crystallinity, surface area, and the surface hydroxyl group's density, could affect the photocatalytic activity of TiO_2. TiO_2 can be used as a photocatalyst for both anatase and rutile crystal structures. The anatase phase is much more active than rutile; however, it requires ultraviolet light to become photocatalytically active. People are currently interested in harnessing sunlight due to the visible light photocatalysis of titanium dioxide. It is, at present, possible to produce visible light active photocatalysts by altering TiO_2 with metals. Nevertheless, due to their potential to serve as recombination sites that lower quantum efficiency, some dopants significantly increase while others decrease the photocatalytic degradation of contaminants [38]. For instance, the recombination of charge at defect sites is attributable to the copper incorporation into TiO_2, which is the cause of the Cu-doped TiO_2 unfortunate catalytic activity, and the high efficiency of W-doped TiO_2 [41]. Co-doping and the creation of stable anatase TiO_2 photocatalysts at high temperatures can both be accomplished with non-metal doping. The fluorine and nitrogen high-temperature stable anatase preparation (F, N), co-doped by a microwave pretreatment, was carried out by other authors in an effective, quick, and simple manner [42]. By co-doping N, F, and P, they also increased the high-temperature stability of the anatase TiO_2 photocatalyst. It is well known, for example, that modifying anatase TiO_2 by hexagonal boron nitride increases the transition temperature of anatase to a rutile, and gets better photocatalytic activity when exposed to sunlight when compared to bare TiO_2. Despite the numerous applications for mesoporous TiO_2 powder and films that have been reported so far, catalyst effectiveness is still hampered by two main deficiencies: (i) both the photogenerated charges rapid recombination, and (ii) activation in the ultraviolet region, which makes up only about 3 to 5% of the whole spectrum of solar, are restricted by its broadband energy. To reduce the TiO_2 photocatalytic activity second deficiency, TiO_2 can be modified with a variety of elements, particularly transition metals and ions of rare earth metal. In order to create cerium titanate (Ce-Ti) porous materials, nanorods, nanoparticles, and cerium-doped TiO_2, multiple earlier studies

have used a multi-approach. The photocatalytic performance of this kind of catalyst is enhanced by the state of band gap created by Ce, which in turn is used as a doping element in TiO$_2$ [43]. Therefore, more research on this subject is required. Titanates, on the other hand, are TiO$_2$-containing compounds with thermally stable, chemically stable, high photocatalytic activity and remarkable selective adsorption [34–46]. At the same time, it is challenging and time-consuming to separate the catalyst from the reaction media. As a result, polymers such as chitosan, cellulose, and others have been utilized as the base material for semiconductors in recent years [47–50]. These polymers act as an interface for charge transfer and lessen ion leakage in the treated water. Chitosan is one of many polymers, but it is particularly popular because of its beneficial characteristics, such as its nontoxicity, biodegradability, biocompatibility, antibacterial properties, and so on [51]. Chitosan's structure is mainly composed of glucosamine and N-acetyl glucosamine. As a result, the amino group within its structure is the primary cause of its affinity to dissolve in acids, as it acts as a cationic polyelectrolyte, causing chitosan to adhere to negatively charged surfaces [52]. Chitosan's amino and hydroxyl groups can also act as active sites during the adsorption process. Chitosan was used previously in the removal of organic pollutant from wastewater [53].

The main objective of this work is to synthesize a highly efficient photocatalytic nanocomposite material, chitosan/silicotitanate (CHMix), for the degradation of some organic dyes present in polluted water. This research also aims to synthesize such a compound using economically feasible materials such as rice husk ash (as a source of silica) and chitosan, along with green synthesis techniques. The primary benefit of this hybrid process is the improvement in chitosan performance and the development of a highly effective wastewater treatment method. Consequently, the CHMix photocatalytic activity is assessed when exposed to sunlight while using reactive blue (RB) and Congo red (CR) as models. This work can provide a practicable way to create nanocomposite with superior photocatalytic degradation and high stability.

2. Results and Discussion

2.1. Characterization of CHMix Nanocomposite with Respect to Pure Chitosan, Si–Ti (S1, S2, and S3)

2.1.1. FTIR Analysis

The FTIR spectra of pure chitosan, silicotitanate with different molar ratios of Si–Ti (S1, S2, S3), and Si–Ti (S2) crosslinked with chitosan (CHMix) are shown in Figure 1. The infrared spectra of silicotitanate powder (S1, S2, S3) exhibit three separate regions with peaks at the wave numbers 455–961, 1600–2000, and 2800–3500 cm^{-1}, respectively [54,55]. The Si-O-Si stretching modes and the Ti-O-Ti vibration stretching are associated with the first region (455–961 cm^{-1}) [51,56,57]. The second peak refers to the H-O-H bending of pure water [58], whereas the broad peak in the higher wave number region (2800–3500 cm^{-1}) relates to the O-H stretching, indicating the presence of hydronium ions [59–61]. Figure 1 also shows the IR spectrum for pure chitosan and the prepared nanocomposite (CHMix), which has the same characteristics, with some notable intensity peaks shifting and the appearance of peaks due to N-H and O-H bending vibration shifts. Due to the chemical modification of chitosan (CHMix), the new bands (Figure 1) observed at 1354, 1000–1250, and 455 cm^{-1} are due to in-plane OH, Si-O-Si bending, and O-Si- or O-Ti bending, respectively [62]. These outcomes demonstrate that the amino and hydroxyl groups are involved in composite formation, which characterize the chitosan silicotitanate nanocomposite.
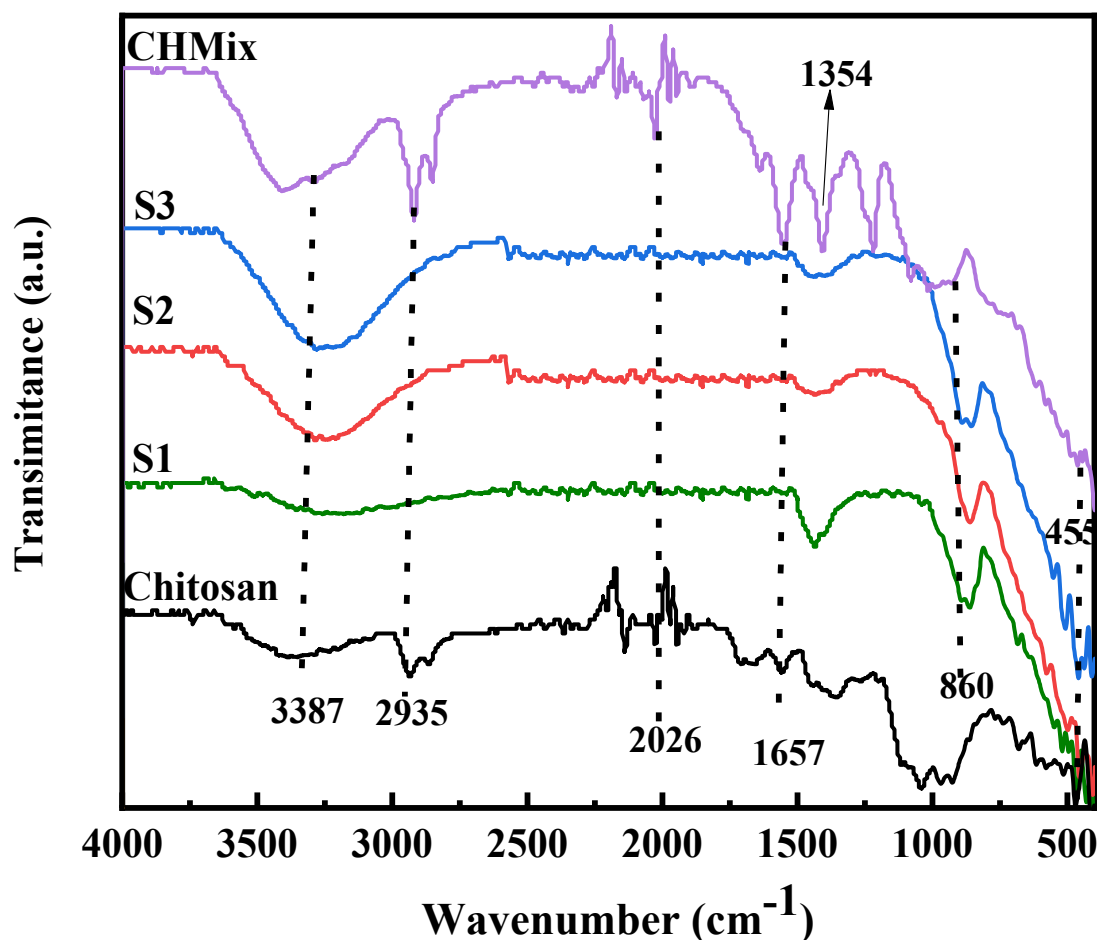
Figure 1. FTIR pattern for pure chitosan, silicotitanate with different molar ratios of titanium (S1, S2, S3), and S2 crosslinked with chitosan (CHMix).

2.1.2. X-ray Diffraction Analysis

X-ray diffraction profiles were carried out to characterize the phase structure of pure chitosan, silicotitanate with different molar ratios (S1, S2, S3), and Si–Ti(S2) crosslinked with chitosan (CHMix), as presented in Figure 2. The figure shows four main crystalline peaks for S1, S2, and S3 at 2θ equal to 12.19°, 28.22°, 32.31°, and 47.9°, which correspond to (100), (113), (300), and (606) of silicotitanate (JCPDS 47-0591) [63]. The intensity of the strongest peaks at 28.22° and 47.9° increase with the increasing titanium molar ratio, and indicate that titanate is in the anatase phase according to card number 21-1272 [63]. An XRD of pure chitosan revealed strong peaks at 2θ around 17.7° (broad), indicating that chitosan exist as an anhydrous crystalline phase [64,65]. After the crosslinking reaction of chitosan with 2 M Si–Ti (CHMix), and after comparison with the XRD pattern of pure chitosan, new peaks were detected in the nanocomposite (CHMix) due to H-bonding with the functional group of chitosan. The broad chitosan peak around 17.7° became negligible in the nanocomposite, and new peaks around 2θ equal to 20.4° and 21.63 appeared. Additionally, two peaks were identified at the 2θ = 29.5° (200) and 36.06° (130) planes relating to silicotitanate [66], indicating a strong interaction between chitosan and Si–Ti nanoparticles (S2). Table 1 presents values of d-spacing, and and Full width half maximum (FWHM) before and after the crosslinking reaction which are computed using the modified Scherer equation [66].
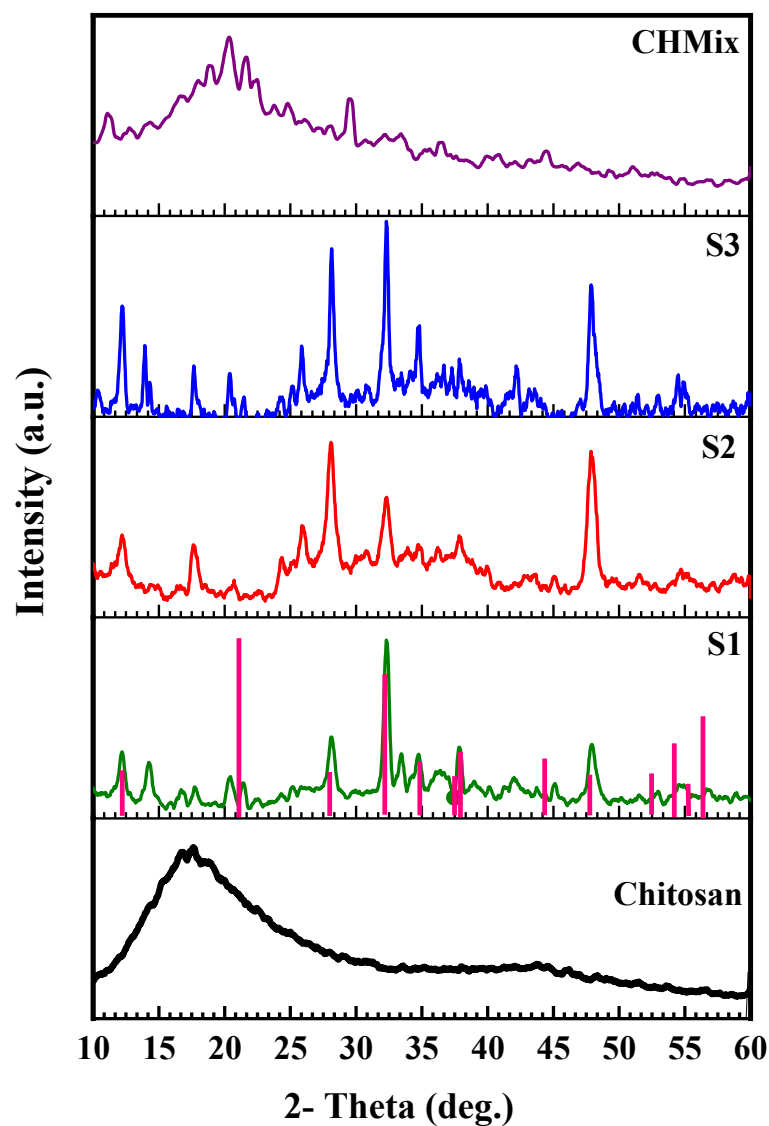
Figure 2. X-ray diffraction analysis (XRD) patterns for different prepared samples.

Table 1. d-spacing and FWHM of S1, S2, S3, and CHMix nanocomposite material.

S1			
Pos. (2θ°)	**d-spacing (A°)**	**FWHM left (2θ°)**	**Rel. Int. (%)**
12.19	7.25	0.35	22.75
14.23	6.22	0.35	20.95
20.40	4.35	0.47	11.15
21.44	4.14	0.35	12.52
28.22	3.16	0.47	21.72
32.31	2.77	0.29	78.83
37.86	2.37	0.23	29.72
47.90	1.89	0.47	27.17
S2			
Pos. (2θ°)	**d-spacing (A°)**	**FWHM left (2θ°)**	**Rel. Int. (%)**
12.22	7.24	0.70	5.06
17.56	5.04	0.47	6.80
25.96	3.43	0.70	4.90
28.07	3.17	0.47	16.83

Table 1. *Cont.*

32.31	2.77	0.59	8.35
47.94	1.89	0.59	14.80

		S3	
Pos. (2θ°)	**d-spacing (A°)**	**FWHM left (2θ°)**	**Rel. Int. (%)**
12.22	7.23	0.29	20.16
13.94	6.35	0.17	12.52
17.66	5.02	0.35	9.54
20.44	4.34	0.35	7.89
25.83	3.44	0.35	9.47
28.12	3.17	0.23	26.16
32.31	2.77	0.23	34.85
34.73	2.58	0.35	12.61
47.86	1.90	0.47	21.46

		CHMix	
Pos. (2θ°)	**d-spacing (A°)**	**FWHM left (2θ°)**	**Rel. Int. (%)**
20.41	4.35	0.70	61.02
21.63	4.10	0.35	71.71
29.50	3.02	0.14	100.00
36.40	2.46	0.17	75.09

2.1.3. Scanning Electron Microscope Analysis

SEM was used to study the possessions of various treatments on the morphology of pure chitosan, S1, S2, S3, and (CHMix) nanocomposite materials, as shown in Figure 3. As seen with high magnification, the prepared materials (S1, S2, and S3) were rough and aggregation occurred; the particle agglomeration was a large granule shape, signifying that the silicotitanate particles were acutely agglomerated. In the case of nanocomposites (CHMix), irregular shaped materials with random orientation were clearly observed on the polymer surface in comparison with pure chitosan, indicating that nanocomposites (CHMix) were completely formed from the binding of inorganic silicotitanate with the organic chitosan polymer; i.e., different from pure chitosan, which has an almost smooth surface.
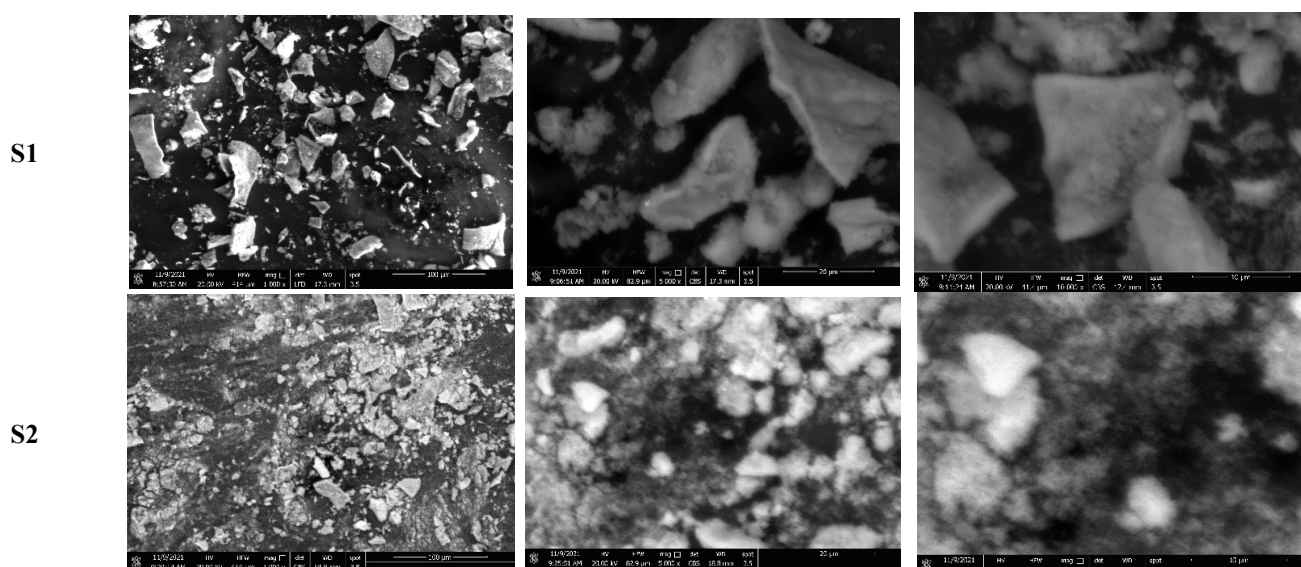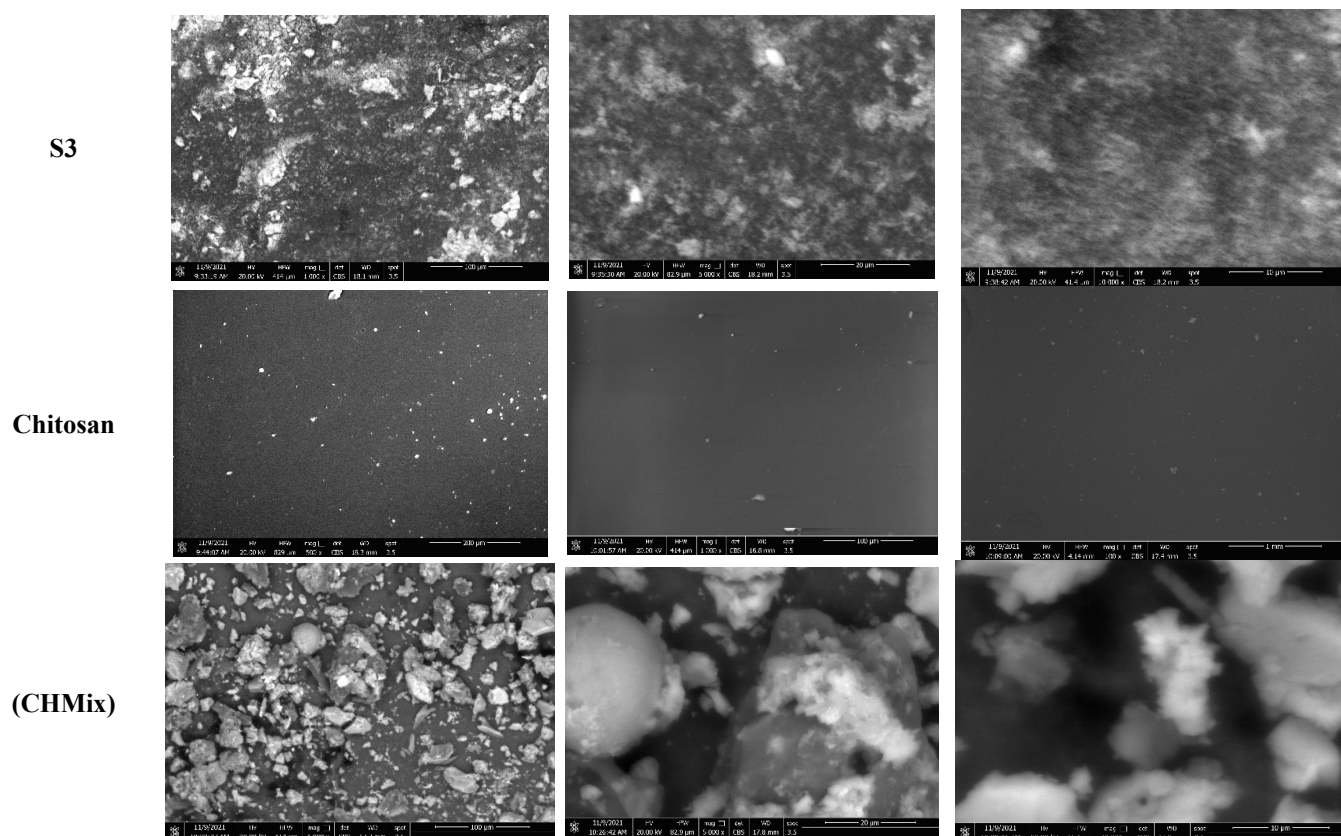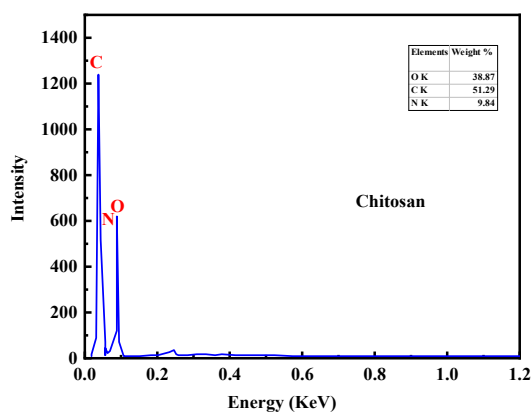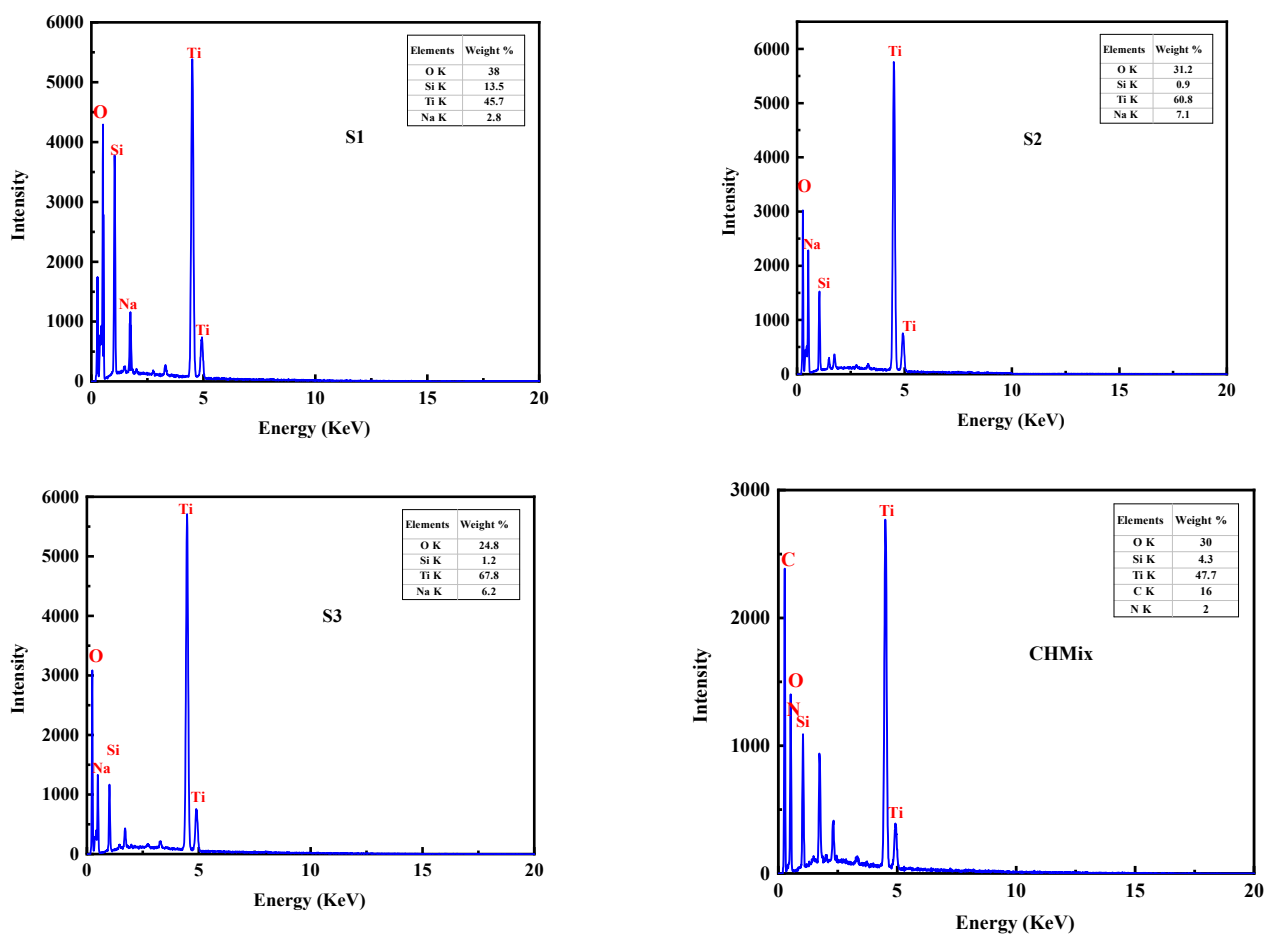

Figure 3. *Cont.*

Figure 3. Scanning electron microscopy images of pure chitosan, silicotitanate with different molar ratios of titanium (S1, S2, S3), and S2 crosslinked with chitosan (CHMix).

2.1.4. Energy Dispersive X-ray Analysis

EDX analysis was employed to confirm the presence of major constituents of pure chitosan, S1, S2, S3, and CHMix nanocomposite material (as presented in Figure 4). In the case of pure chitosan beads, the characteristic peaks of carbon, nitrogen and oxygen were observed, while in S1, S2, and S3 nanoparticles, EDX consists essentially of silicon (Si), titanium (Ti), oxygen (O), and a small peak of sodium (Na). The sodium is from the silica solution, which was extracted from rice husk ash. The very high peak of Si and Ti in the EDX spectrum suggests that the hybrid nanocomposite consists predominantly of silica and titanium. The carbon in CHMix is from the chitosan polymer.


Figure 4. *Cont*.

Figure 4. EDX analysis of pure chitosan, silicotitanate with different molar ratios titanium (S1, S2, S3), and S2 crosslinked with chitosan (CHMix).

2.1.5. Zeta Potential

The surface charges of pure chitosan, S1, S2, S3, and CHMix nanocomposite material affecting anionic dye adsorption were further analyzed by zeta potential under the pH ranges of 2.0–9.0, and surface charge distribution is displayed in Figure 5. Alternatively, chitosan has several-NH_2 and -OH groups which give different surface charges upon protonation or vice versa under acidic and alkaline mediums, respectively. Conversely, as the pH increases (pH = 5), further amine groups grow to be available in the chitosan chain for dative bonding (electron donor) with silica cations, thus reducing the electrostatic repulsion and supporting the stabilization of the Si–Ti NPs at smaller dimensions owing to the increase in the number of nucleation sites [67]. The two anionic dyes (Congo red and reactive blue) applied in this study have different numbers of SO_3^- groups. Thus, Congo red and reactive blue dyes and chitosan would have dissimilar levels of electrostatic interaction under acidic and alkaline environments [68]. Generally, zeta potentials of chitosan, S1, S2, S3, and CHMix nanocomposite are positive in an acidic environment and negative after pH 7. Zeta potentials of chitosan, S1, S2, and S3 before the isoelectric point were more positive than those of crosslinked CHMix nanocomposite. These results indicated a decrease of the surface charge with an increasing pH level [68].
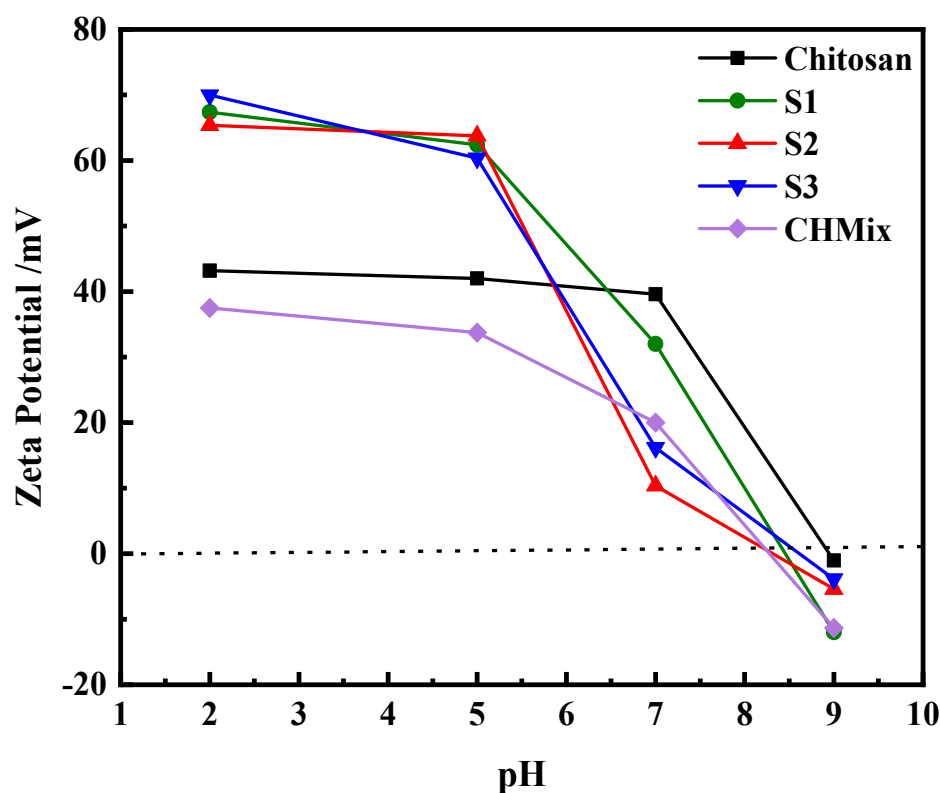
Figure 5. Zeta potential curves of pure chitosan, S1, S2 and S3, and CHMix nanocomposite solutions at different pH.

2.1.6. Surface Area Measurements

From the N_2 adsorption–desorption isotherm (Figure 6), we noticed that all fabricated silicotitanate (S1, S2, and S3) revealed a mesoporous structure of type IV isotherms [69,70]. The hysteresis is present, along with capillary condensation in a Type IV a isotherm [70]. This happens when the pore width surpasses a specific critical width, which is dependent on the adsorption system and temperature; for example, for nitrogen and argon adsorption in cylindrical pores at 77 K and 87 K, respectively, hysteresis starts to occur for pores wider than 4 nm. In addition, the Brunauer, Emmett and Teller surface surface area (BET), the pore volume (Vm), the total pore volume, and the average pore diameter decrease with increasing titanate concentration in silicotitanate (Table 2). This could be rationalized by filling the pores of silica NPs with more titania molecules, which would decrease both the pore volume and the BET surface area. On the other hand, neat chitosan biopolymer showed the lowest BET surface area, pore volume, total pore volume, and average pore diameter with macropores structure. When blending chitosan with silicotitanate (CHMix) in a mole ratio of 2, the BET surface area, the pore volume, the total pore volume, and the average pore diameter increased while retaining the macropore structure.

Table 2. BET, pore volume, and average pore diameter of pure chitosan, S1, S2, S3, and CHMix nanocomposite material.

Parameters	Unit	Pure Chitosan	S1	S2	S3	CHMix
V_m	$cm^3(STP)\ g^{-1}$	0.06	3.23	3.01	1.74	0.19
BET	$m^2\ g^{-1}$	0.28	14.06	13.08	7.55	0.83
Total pore volume	$cm^3\ g^{-1}$	0.01	0.13	0.08	0.05	0.04
Average pore diameter	nm	139.85	38.45	26.37	25.76	63.381
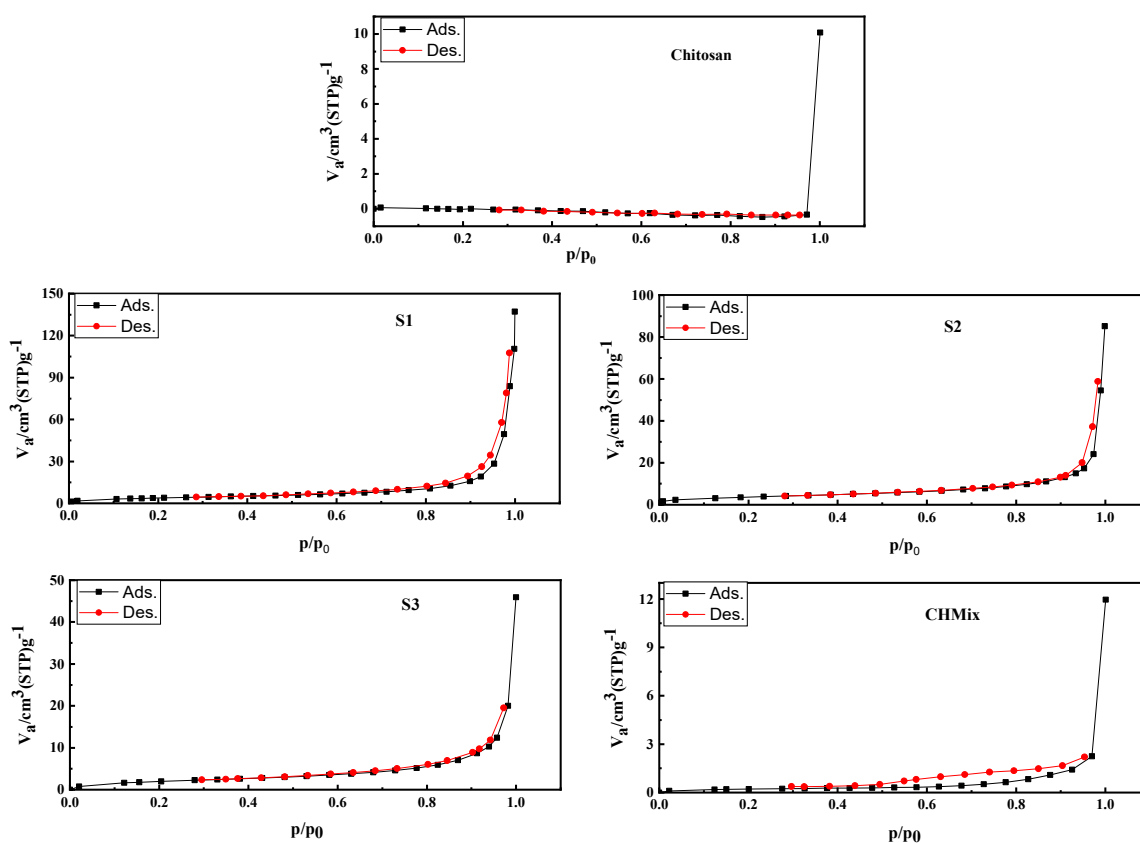
Figure 6. N_2 adsorption–desorption isotherms of pure chitosan, S1, S2, and S3, and CHMix nanocomposite materials.

### 2.1.7. UV–Vis Spectroscopy and Energy Band Gap

The UV–vis spectra of chitosan, S1, S2, S3, and CHMix nanocomposite are shown in Figure 7. In the present study, the UV absorption spectra of S1, S2 and S3 show absorption peaks at 310.9 and 327 nm, 309.7 and 327.6 nm and 307.09 nm, respectively. While the absorption peaks of pure chitosan and CHMix nanocomposite are 278.6 and 296.7 nm, respectively, these values are lower than of nanocrystalline S2 (309.7, 327.6 nm). In addition, the pure chitosan displayed some visible light absorption, which, usually, could be connected to a narrowing of the band gap after the synthesis of the CHMix nanocomposite [71]. The apparent shift in the nanocomposites may be a result of S2 chemical reactions with chitosan significant molecular structure. The corresponding band gap values were obtained by plotting Tauc's plot obtained from absorption spectra function [72,73] against the photon energy (inset in Figure 7) and found 2.80, 2.88, 2.82, and 2.76 eV for S1, S2, S3, and CHMix, respectively. The band gap values of CHMix nanocomposites (Eg = 2.76 eV) were lower than that found for the S2 (Eg = 2.88 eV). As a result of the production of the CHMix nanocomposites, the bonding interactions between chitosan and Si–Ti were validated and made a decrease in band gap, and they were directly associated to an enhancement in photodegradation performance [74].
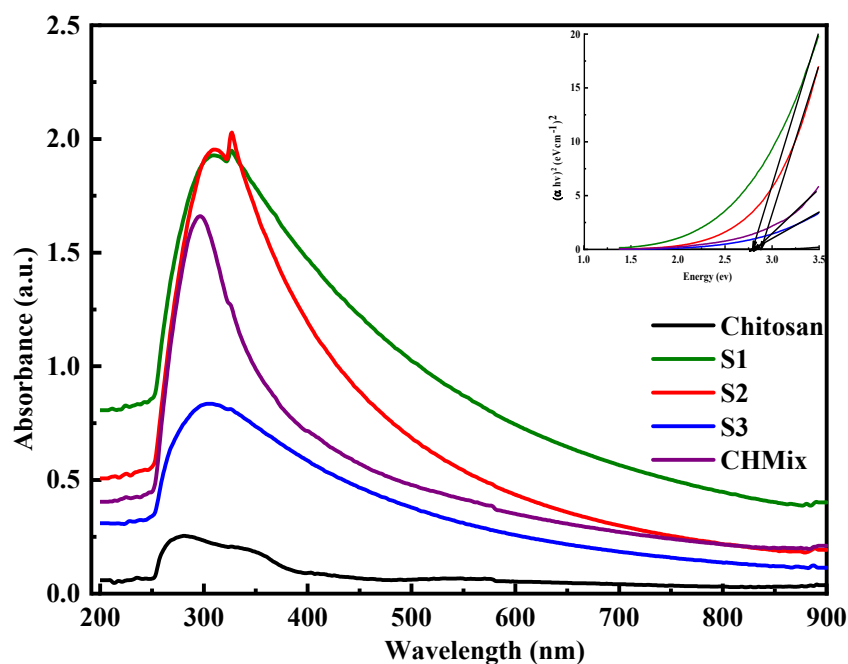
Figure 7. The UV-vis absorption spectroscopy, and Tauc's plot of the prepared samples.

2.2. Dye Adsorption and Photocatalytic Study

Dye removal efficiency of the fabricated samples (chitosan, S1, S2, S3, and CHMix nanocomposite) towards anionic dyes (reactive blue (RB) and Congo red (CR)) was evaluated at neutral pH by examining the adsorption performance as presented in Figure 8A,B. The adsorption efficiency of chitosan towards anionic dyes in Figure 8 was high. The addition of silicotitanate (S2) to give chitosan silicotitanate (CHMix) nanocomposite material caused an increase in the removal efficiency up to (45 and 85%) for RB and CR, respectively. These results may be explained based on the charge of chitosan and silicotitanate, as well as dye molecules. Because of its cationic nature, chitosan exhibited high adsorption efficiency towards anionic dyes (CR and RB). Additionally, with the incorporation of S2 to form CHMix, the adsorption activity increased, Generally, zeta potentials of chitosan, S1, S2, S3, and CHMix nanocomposite are positive at neutral pH. Consequently, it could be hypothesized that the addition of Si–Ti (S2) to chitosan led to a clear increase towards the RB and CR dye removal performance when using the obtained CHMix in comparison with pure chitosan [75]. As a matter of fact, it is possible to conclude that chitosan has a beneficial effect on the discoloration procedure. The charge separation caused by the Si–Ti charge on the chitosan could explain the increased discoloration. The main role of chitosan are the electron transport from Si–Ti NPs, and the limiting of the electrons–holes pair recombination [76]. A large number of photoreactive species were formed as a result of longer-lasting electron–hole pairs. Additionally, the dye molecules are concentrated around the catalyst due to the adsorption capacity of chitosan and the nanocomposite's porous structure, which makes it more probable that the dye molecules will diffuse and transfer to the external below a concentration slope. As a result, both the dye sufficiency and the degradation percentage are raised. Throughout all circumstances, there is still a small amount of dye in the solution; this shows that the process's blocking of photocatalytic active sites makes it difficult for the residual organic matter or intermediate products to degrade completely [76,77]. The findings demonstrate a significant variation in degradation effectiveness by CHMix.

A

B
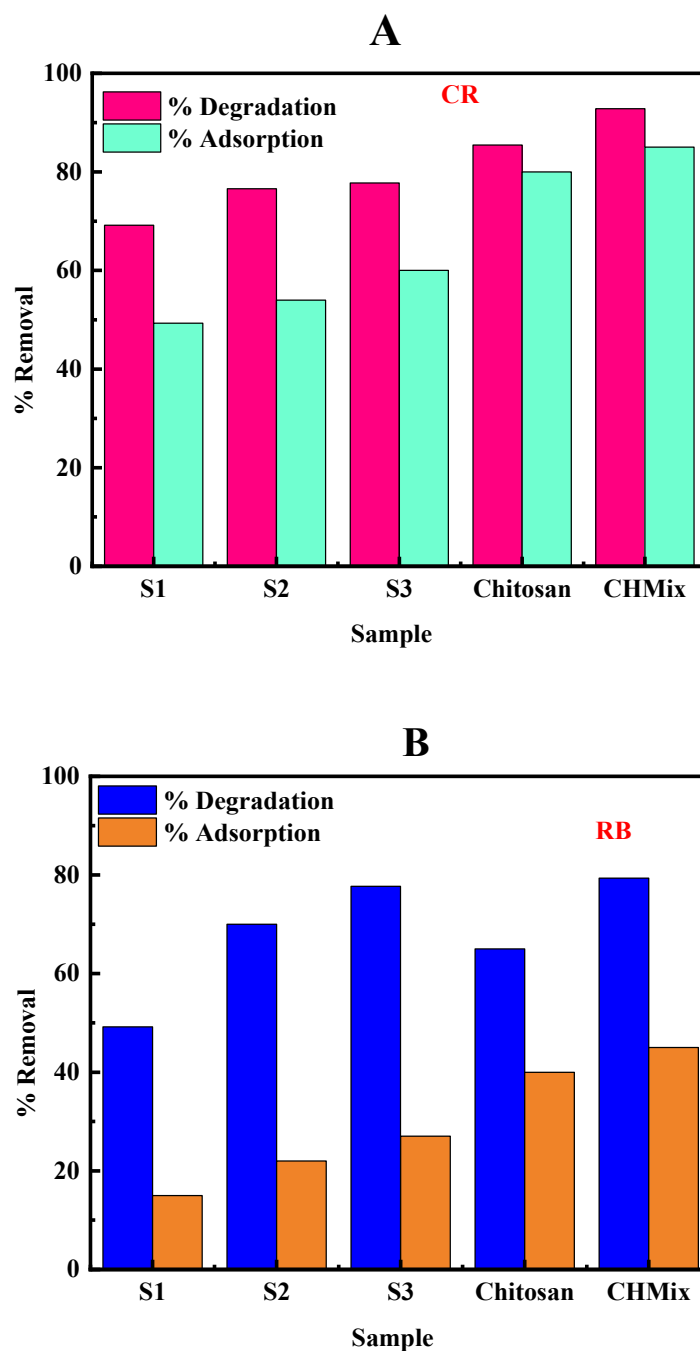
Figure 8. The adsorption efficiency and photocatalytic degradation of CR (**A**) and RB (**B**) dyes (10mL, 33 mg/L CR and RB, 0.05 g of pure chitosan, S1, S2, and S3, and CHMix nanocomposite material).

2.2.1. Effect of Dose on Photocatalytic Activity

The photodegradation effectiveness is influenced by catalyst dosage. In a 50 mL solution of reactive blue (RB) and Congo red (CR), with a concentration of 100 mg L^{-1}, pure chitosan, S1, S2, S3, and CHMix doses were dispersed. Figure 9A,B illustrates the relationship between the rate of photodegradation and the dose of pure chitosan, S1, S2, S3, and CHMix. As predicted, the efficiency of photodegradation increased with the increasing dose of catalyst for the reason that more binding sites were available for degradation. The degradation sharply increases the behavior of the CHMix composites at different doses with RB and CR. The other catalyst, on the other hand, exhibited promising degradation behavior at 100 mg L^{-1}, which is why CHMix was chosen as the standard for subsequent experiments. As a result, the composite CHMix has the highest catalytic ability to degrade

RB and CR. CHMix can degrade CR and RB dyes by more than 95% and 90% in 5 h. This indicates that the active groups that are able to degrade the CR and RB dyes are readily obtained through the activation procedure. However, when nanoparticles of Si–Ti are directly cross-linked with chitosan, the rate of discoloration enhances due to the use of nanoparticles in the production of nanocomposites [43]. In order to investigate dye removal, CHMix nanocomposite materials were used as photocatalysts in the subsequent experiments. and the most effective dose is 50 mg.
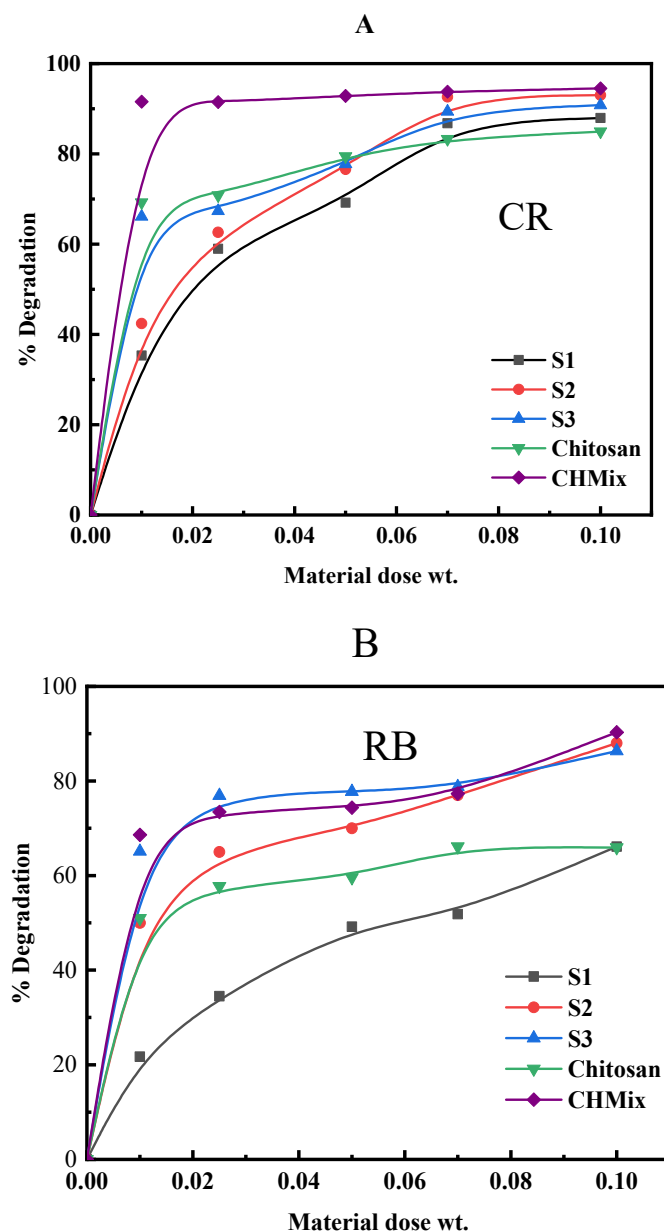

Figure 9. The effect of material dose on the CR (**A**) and RB (**B**) dye photodegradation by pure chitosan, S1, S2, and S3, and CHMix nanocomposite material (dosage of 0.01, 0.025,0.05,0.07, and 0.1 g). The CR and RB concentration was 100 mg/L, CR and RB dyes were at a pH of 6, and the degradation time was 360 min.

2.2.2. The Effect of Dye Solution pH on Photocatalytic Degradation

The pH level significantly affects how well the photocatalyst works. To modify the pH of dye (CR and RB) solutions, sodium hydroxide and hydrochloric acid were used in this experiment. Figure 10 shows the effects of a pH ranging from 2–10 and a dye starting concentration of 100 ppm on a 50 mg CHMix nanocomposite in a 20 mL solution

of dyes (CR) and (RB) over the course of three hours. The degradation effectiveness of CR and RB increases as the pH increases from acidic to alkaline values, and then gradually decreases after pH 9. The nanocomposite catalysts showed much higher degradation rates for CR (95%), compared to RB (56%), which can be explained by the abundant functional groups and the photocatalytic reaction that occurred. This high photocatalytic activity is due to the remarkable synergistic effect of the molecule interfacial layers on (CR) adsorption [78–80]. Titania–silica/cobalt ferrite photocatalyst has previously demonstrated similar behavior [81]. The pH level has a significant impact on the photocatalyst's surface charge properties. In an alkaline solution, a photocatalyst's surface can be negatively charged; however, in an acidic solution, it posed positive charges [82]. At alkaline pH values, the interaction between photogenerated holes and hydroxide ions (OH) to produce hydroxyl radicals (OH) is most likely improved, which, in turn, would support the photocatalytic degradation process [81].
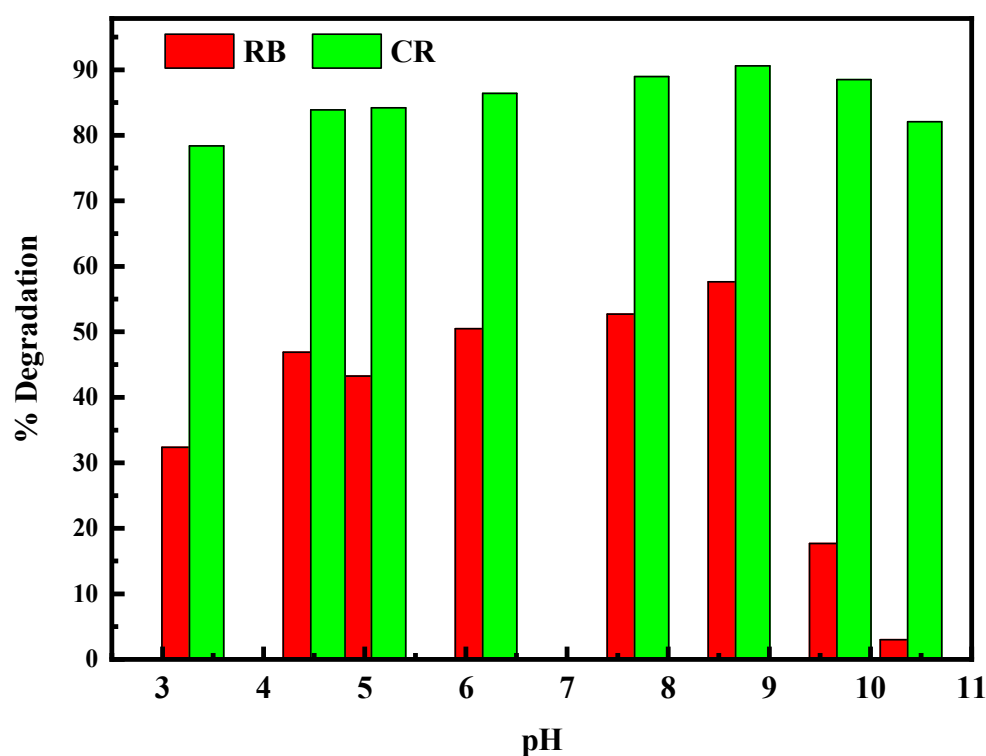

Figure 10. Influence of solution pH range (2–10) on photodegradation of CR and RB dyes on CHMix (with a dosage of 50 mg, a CR and RB concentration of 100 ppm, and a degradation time of 180 min).

2.2.3. Effect of Degradation Time

The effect of contact time on the degradation of CR and RB by CHMix nanocomposite material in sunlight, concentrated sunlight, and in the presence of H_2O_2 at optimal pH and adsorbent dosage was investigated. This investigation's findings are summarized in Figure 11. According to the findings, the dye degradation percentage increases significantly during the early contact time. They begin to increase slowly after 25 min and reach near equilibrium at about 120 and 175 min for CR and RB, respectively. The equilibrium time between the dye and the photocatalyst is therefore optimized to 120 min for CR and 175 min for RB. When the degradation efficiency with and without H_2O_2 were compared, it was shown that the intensity of the concentrated light improves the ability of the photocatalyst; additionally, at early intervals, H_2O_2 improves the degradation ability of the nanocomposite sites and reaches near equilibrium after about 30 min. The combined effects of photodissociation of H_2O_2 with light and on the photocatalyst surface, as well as the complex transport of highly reactive hydroxyl radical (•OH) in the reactant mix, may be responsible for the enhanced photodegradation of dyes with nanocomposite material in the

presence of H_2O_2. The crucial step is the photolysis of H_2O_2 to produce hydroxyl radicals, which can then be used to interact with organic compounds [83]. During photocatalysis, H_2O_2 may be used as an electron scavenger. In the molecular orbital of the photocatalyst, the hydroxide ion produced during H_2O_2 electron scavenging may combine with holes (h^+), reducing electron–hole recombination [84]. The hydroxyl radical is more efficient at oxidizing organic molecules than the superoxide ion (O_2^-) that was produced during the reaction [85]. It is obvious that H_2O_2 can interact with both oxidized and reduced catalyst surfaces, and that both the catalyst and H_2O_2 can undergo redox reactions simultaneously. Additional hydroxyl radicals and ions are produced as a result of such reactions, which act as electron/hole hunters and interact with organic compounds. The photocatalytic reaction may also be enhanced by hydroxyl, superoxide, and perhydroxyl radials that tend to react on the catalyst surface. The increase in the overall photodegradation rate may be explained by such a cycle of reactions.
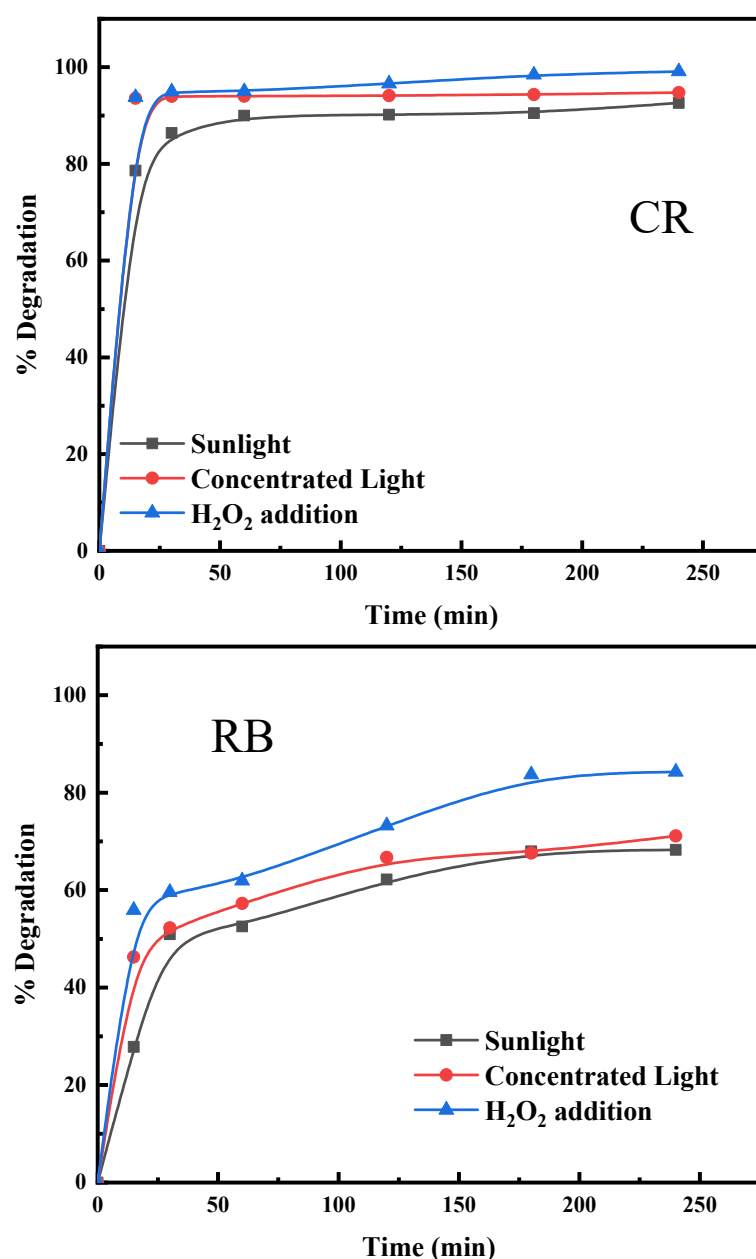
Figure 11. The effect of contact time on CR and RB degradation in sunlight and concentrated sunlight in the presence of H_2O_2 on CHMix(dosage of 0.05 g, a CR and RB concentration of 100 ppm at pH 6).
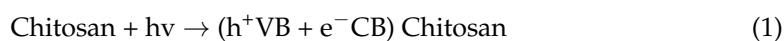
2.2.4. Scavenger Experiments and Reaction Mechanisms

In order to propose a photocatalytic mechanism for the degradation of CR and RB, the key active species such as $^\bullet OH$, $^\bullet O_2$, h^+, and H_2O_2 were investigated. Figure 12 shows the radical experiment results against CR and RB photodegradation using CHMix nanocomposite under sunlight irradiation. It can be observed that the photocatalytic performance was inhibited to 70% and 15% after the addition of the p-benzo quinone scavenger to CR and RB dye solutions, respectively. This signified that the $^\bullet O_2^-$ radicals play a crucial role in CR and RB photodegradation. In addition, the photodegradation rate of CR and RB was significantly decreased after the addition of EDTA-2Na and $AgNO_3$ scavengers into the reaction solution, verifying the major role of h^+ and e^- species in the photoreaction [69]. In contrast, the $^\bullet OH$ and H_2O_2 displayed no influence on the CR and RB photodegradation performance, where the photodegradation efficiency was still high (88, 87, and 85% for CR and 62, 50 and 48% for RB), in spite of the addition of methanol, isopropanol and Fe (II) to the reaction, respectively. According to the above results, the power of the reactive species can be ordered as follows: $^\bullet O_2 > e^- > h^+ > H_2O_2 > {}^\bullet OH$.
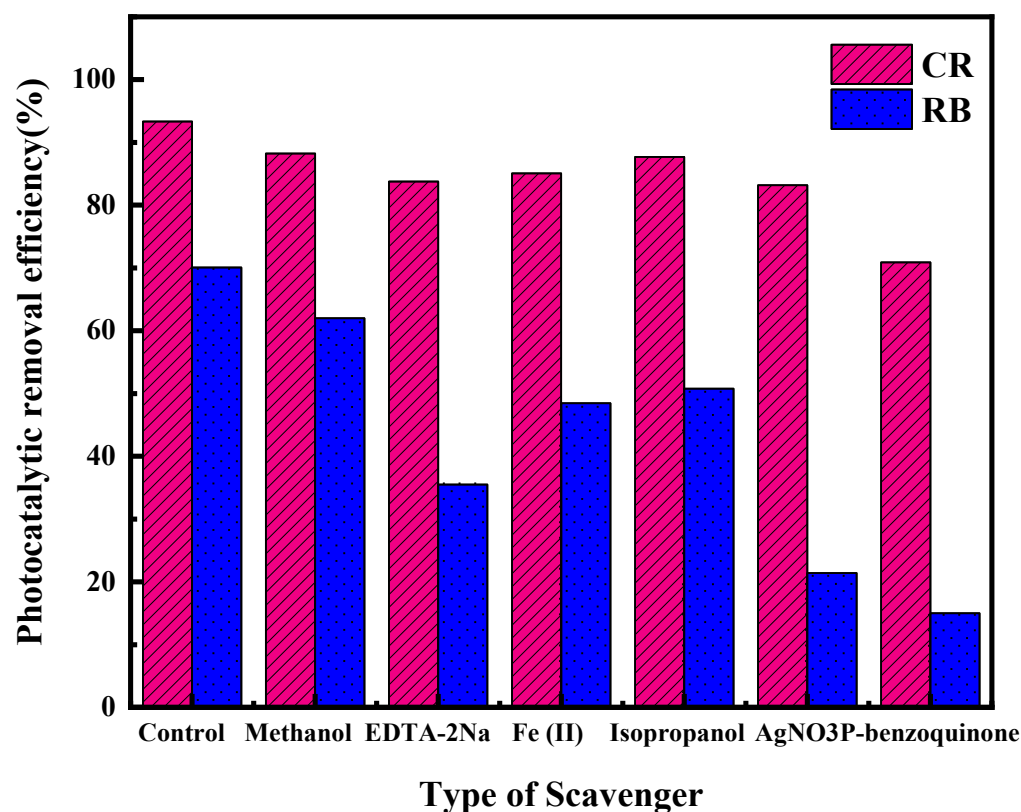

Figure 12. Trapping experiment of CR and RB oxidation (CHMix dosage of 1 g/L, CR and RB concentration of 100 ppm, and a pH of 6.2).

The mechanism of organic dye degradation reactions by photocatalysis has previously been described. The photocatalyst (such as a semiconductor) captures light energy that is greater than the material's band gap during photocatalysis. As soon as the light hits the photocatalyst surface, the electrons (e^-) in the valance band become energized and move up into the conduction band. A positive hole forms on the valence band (h^+VB) when the electron is in the conduction band (e^-CB), as shown in Equations (1)–(10):

$$\text{Chitosan} + \text{hv} \rightarrow (h^+VB + e^-CB) \text{ Chitosan} \tag{1}$$

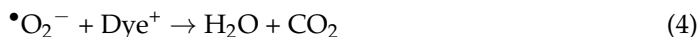$$\text{S2} + \text{hv} \rightarrow (h^+VB + e^-CB) \text{ S2} \tag{2}$$

Superoxide radicals are now produced by the energized electrons' reaction with O_2 in the conduction band, as demonstrated in Equation (3):

$$(e^- CB)S2 + O_2 \rightarrow {}^{\bullet}O_2{}^- \tag{3}$$
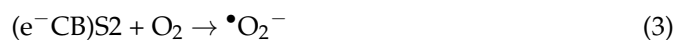
According to Equation (4), these radical oxygen species have the ability to convert contaminants (dyes) into CO_2 and H_2O.
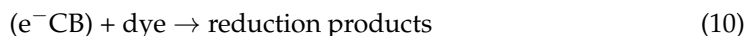
$$ {}^{\bullet}O_2{}^- + Dye^+ \rightarrow H_2O + CO_2 \tag{4}$$

The positive hole oxidizes water to produce hydroxyl and hydrogen ions in the valence band, as shown in Equation (5).

$$H^+(VB) + H_2O \rightarrow OH^- + H^+ \tag{5}$$
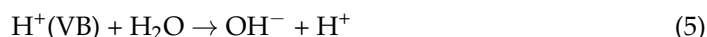
The pollutants (dyes) can be mineralized by the hydroxyl ions created in the afore-mentioned reaction, changing them into the H_2O and CO_2 provided in Equation (6).

$$OH^- + Dye^+ \rightarrow + H_2O + CO_2 \tag{6}$$
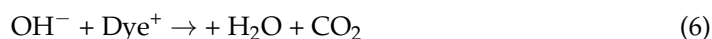
As shown in Equations (7)–(10) [86,87], the superoxide radicals produced can also be used for additional degradation processes:

$$ {}^{\bullet}O_2{}^- + H^+ \rightarrow HO_2 \tag{7}$$

$$H_2O_2 \rightarrow 2{}^{\bullet}OH \tag{8}$$

$$ {}^{\bullet}OH + dye \rightarrow dye\ (ox) \tag{9}$$

$$(e^- CB) + dye \rightarrow reduction\ products \tag{10}$$

2.3. Applications of Sunlight Energy for Real Wastewater

To degrade real wastewater polluted by CR and RB, CHMix nanocomposite material was used. The degradation of CR and RB in sunlight and concentrated sunlight by nanocomposite material was investigated at optimal pH, time, and adsorbent dosage. This investigation's findings are summarized in Figure 13. The results for CR and RB were 88.4 and 89.1%, for the sunlight photocatalytic treatment, and 92.3 and 90.6% for the concentrated sunlight photocatalytic treatment, respectively. The photodegradation results show that the electrical conductivity (EC) of polluted water increases with photocatalytic treatment, as shown in Figure 13 and Table 3. The electrical conductivity (EC) increased from 1527 to 3090 and 3205 mS/cm in sunlight and concentrated sunlight photocatalytic treatments, respectively. These values are attributed to the formation of free radicals during the photocatalytic process. These results verified that CHMix composite demonstrated good photocatalytic efficiency, comparable and, in some cases, better than other comparable systems [72,88–91], as indicated in Table 4. Because of the improvements in degradation efficiency towards CR and RB, the CHMix nanocomposite photocatalyst is a promising photocatalyst for wastewater treatment.
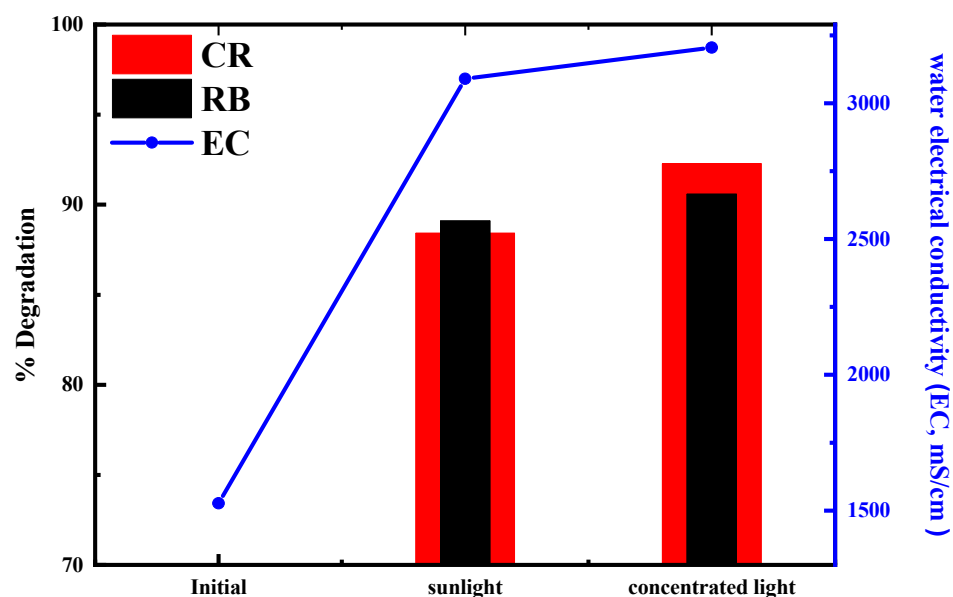
Figure 13. Real wastewater treatment in the presence of sunlight and concentrated sunlight by using CHMix (a dosage of 1 g/L, CR and RB concentrations of 100 ppm, and a pH of 6.2).

Table 3. Physico- chemical analysis of wastewater samples in sunlight and concentrated sunlight by CHMix nanocomposite material.

	Initial Concentration	Concentrated Light	Sunlight
EC (μs/cm)	1527.00	3205.00	3090.00
PH	7.39	6.22	6.40
CO_3	0.00	0.00	0.00
HCO_3 ppm	12.20	106.75	76.25
Cl ppm	152.13	152.13	152.13
TH ppm	441.00	284.20	343.00
Ca ppm	98.00	35.30	39.20

Table 4. Comparison of the photocatalytic performance of CHMix with other reported previous works for the catalytic degradation of CR and RB.

Catalyst	Catalyst Dosage (g/L)	Pollutant Concentration	Light Source	Time Photo (min)	Major ROS	Efficiency (%)	References
Silica-coated Ag_2WO_4/Ag_2S	1.0	Congo red (20 mg/L)	200 W xenon lamp	140	H_2O^2, $^{\bullet}OH$, h^+	99.5	[72]
AgI–Ag_2S@g-C_3N_4	0.5	Congo red (10 mg/L)	500 W xenon lamp	50	h^+	94.2	[88]
Fe_2O_3/porous SiO_2	1.0	Congo red (20 mg/L)	400 W metal halide Lamp	180	$^{\bullet}OH$	88	[89]
CHMix	1.0	Congo red (20 mg/L)	under concentrated solar light	120	$^{\bullet}O_2$, e^-, h^+, H_2O_2	92.3	This work
TiO_2/the Fenton's reagent	1.0	Reactive blue 30 mg/L	Fresnel lens to concentrate solar energy	120	H_2O_2, $^{\bullet}OH$, h^+	50	[90]
V_2O_5	0.6	Reactive blue 25 mg/L	under solar light irradiation	80	H_2O_2, $^{\bullet}OH$	97	[91]

Table 4. *Cont.*

Catalyst	Catalyst Dosage (g/L)	Pollutant Concentration	Light Source	Time Photo (min)	Major ROS	Efficiency (%)	References
CHMix	1.0	Reactive blue 20 mg/L	under concentrated solar light irradiation	120	$^\bullet O_2$, e^-, h^+, H_2O_2	90.6	This work

2.4. Stability and Reusability Measurements

Stability and reusability tests were carried out to illustrate the practical application of CHMix nanocomposite as it had been developed Figure 14. In these experiments, five cycles of CR and RB dye photodegradation were conducted using CHMix nanocomposite under the identical conditions. After each round of degradation, the CHMix photocatalyst was separated using a centrifuge [92,93]. The photocatalytic degradation performance maintained (at 65% for CR and 20.4% for RB) after five measurement cycles. The CHMix nanocomposite showed moderate stability and recycling after the fifth cycle, though there was a high decrease (28.5% and 50%) in photocatalytic degradation performance against CR and RB dyes, respectively, compared with the first cycle as shown in Figure 14. The significant decline in the photocatalytic efficiency was explained by catalyst loss and the reduction of active sites on the CHMix surface by reactive intermediates that can be owing to the limited covering of catalytic active sites [94].
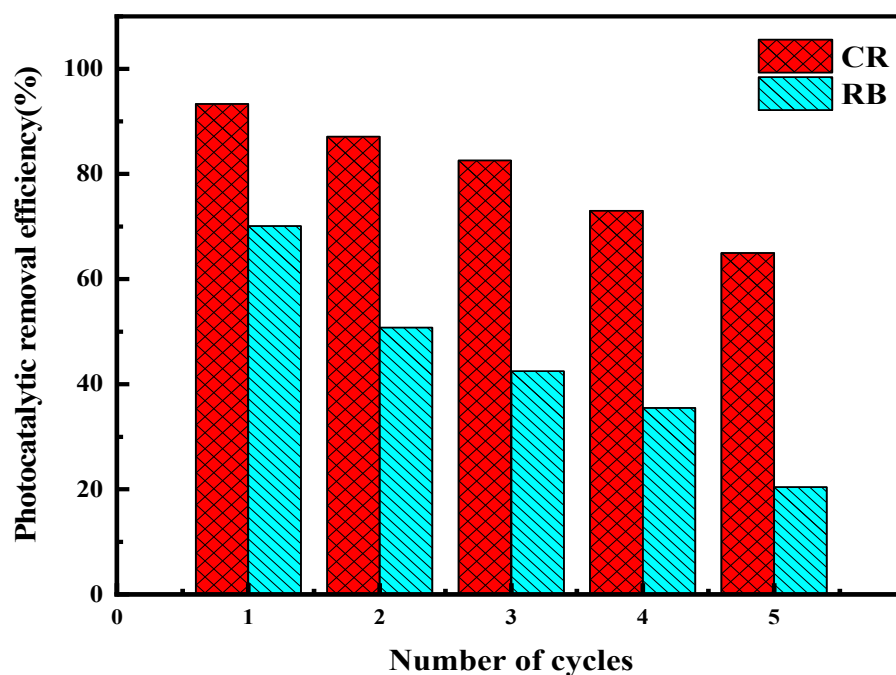
Figure 14. Stability and reusability studies for CHMix nanocomposite using five cycles of CR and RB degradation under sunlight illumination (time = 180 min, catalyst dosage = 1 g/L, pH = 6.2, CR and RB concentration = 100 ppm).

3. Experimental

3.1. Chemical and Reagents

The chemicals used in this research were all of analytical grade and were not purified before use. Rice husk (Giza 78) was collected from the East Nile Delta, Egypt. Chitosan (MW = 8.96×5 g/mole, degree of deacetylation = 40%) was obtained from SE Chemical Co., Ltd., Japan. Titanium (IV) 2-ethylhexyl-oxide, (95%), CAS (1070-10-6) solution was purchased from Alfa Aser, Germany. Reactive blue and Congo red were purchased from R & M chemicals. NaOH (Mwt = 39.99 g/mol) was purchased from Sigma Aldrich, Sweden.

### 3.2. Green Synthesis of Silicotitanate Nanoparticles (NPs)

First, the silicon suspension was prepared by washing rice husk with distilled water, drying it at 60 degrees Celsius, crushing it into a fine powder, and then burning it for eight hours at 900 degrees Celsius to produce rice husk ash. Then, 5.5 g of the rice husk ash was transferred into a 0.5 L stoppered flask containing an 18% NaOH solution, and the mixture was refluxed at 120 °C for two hours before being filtered through filter paper. Second, to make silicotitanate nanoparticles, 10 mL of Tween 80 was mixed with 100 mL of silica solution filtrate. Then, different molar ratios (1, 2, and 3 M) of titanium (IV) 2-ethylhexyl-oxide were added to the previous silica solution. The mixture solution was then heated at 80 °C for 24 h while being constantly stirred. The product was centrifuged, washed several times with deionized water, and dehydrated in an oven, in air, at 80 °C for 24 h until it reached a fixed weight, before being burned at 500 °C for 3 h to remove any remaining organic compounds. The precipitates are denoted by acronyms derived from the Si–Ti molar ratio (shown as S1, S2, and S3, which represent Si–Ti prepared with 1, 2, and 3 molars of titanium (IV) 2-ethylhexyl-oxide, respectively).

3.3. Preparation of Chitosan Silicotitanate Nanocomposite Material

Chitosan solution was initially prepared as follows: 0.5 g of chitosan polymer was dissolved in 100 mL of distilled water, and 2 mL of acetic acid were added and mixed thoroughly. Then, 100 mL of chitosan solution was intercalated using the 2 molar ratios of silicotitanate NPs as follows: in 12 mL of titanium (IV) 2-ethylhexyl-oxide solution and 10 mL distilled water, 10 mL of silicon solution and 1 mL of Tween 80 were dispersed. The previous suspension was treated with 0.08 g ammonium persulfate and heated at 80 °C for 3 h. Then, 100 mL of previously prepared chitosan solution was added, and the process was repeated for another 2 h at 50 °C. After mixing the components, a 5% glutaraldehyde solution was used to crosslink the nanocomposite material. The cross-linked nanocomposite was heated to 50 °C for 24 h, then washed, and dried at 50 °C; and has been denoted by an acronym (CHMix). The synthesis of CHMix nanocomposite material for the degradation of CR and RB dyes isshown in Scheme 1.

3.4. Characterization Techniques

FTIR spectroscopy was used to investigate the interaction of pure chitosan, silicotitanate (S1, S2 and S3) NPs, and CHMix. The procedure was carried out at a rate of 30 scans per minute using a Nicolet Avatar (Waltham, MA, USA) 230 spectrometer to verify infrared spectra with wave numbers ranging from 400 to 4000 cm^{-1}. X-ray diffraction analysis (XRD) analysis was carried out using the database of the Joint Committee on Powder Diffraction Society (JCPDS). A field emission scanning electron microscope was used to examine the morphology of the chitosan–silicotitanate composite (Zeiss Auriga, Padua, Italy). The elemental composition was determined using an EDX XL30 SFEG from Phillips in the Netherlands. Zeta potentials of pure chitosan, S1, S2, S3, and CHMix samples were determined by means of electrophoresis using a MalvernZetasizer 3000. N$_2$ adsorption and desorption measurements were measured on Q adsorb evo equipment (BELSORP-minix (S/N: 10039, version 1.1.3.1, Osaka, Japan) to evaluate the texture of synthesized materials through the sorption system, and the sample was degassed at 80 °C for 24 h. The absorbance spectra of the fabricated materials was measured using UV-vis spectrum(Elico EI 301E, Telangana, India) in the wavelength range of 200–900 nm.
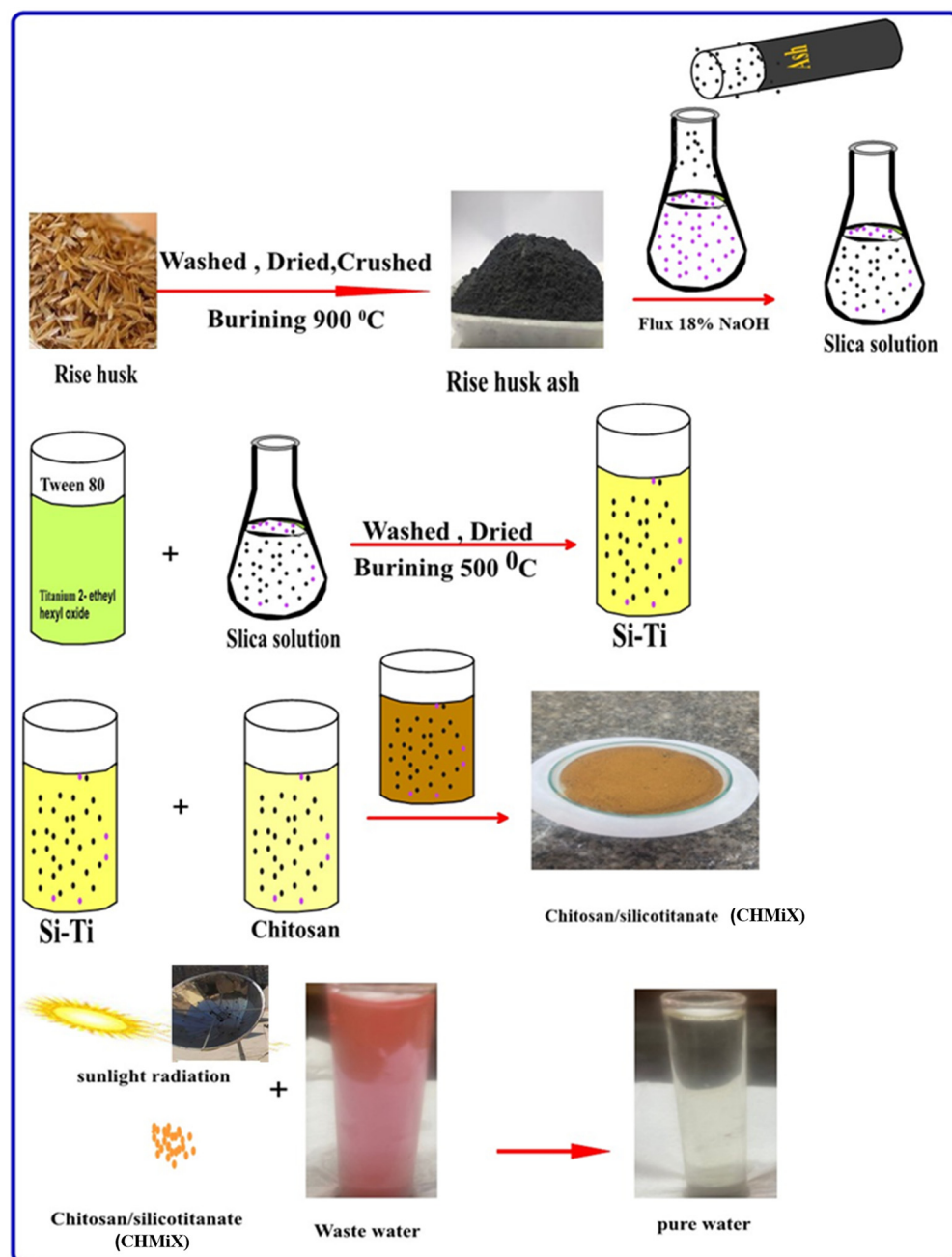
Scheme 1. Illustration synthesis of CHMix nanocomposite material for the degradation of Congo Red (CR) and Reactive Blue (RB) dyes.

3.5. Photocatalytic Degradation

A batch experiment was used to conduct photocatalytic tests. For two months during September through October, all photocatalytic tests were conducted on sunny days between 8:30 a.m. and 3:00 p.m. under the same conditions (the reaction time was 6 h). CHMix nanocomposite (0.05 g) was added to 0.02 L of the reactive blue (RB, 33 mg L^{-1}) solution and Congo red (CR, 33 mg L^{-1}) solution and agitated for a period of time in the dark at room temperature (25 °C) for 1 h to investigate the composite's adsorption behavior. Due to the complex molecular structure of Congo red, a less concentrated solution was used. A higher concentration would make the process take a slightly longer time. A UV-Vis spectrophotometer was used to determine the dye concentration after the sample was collected over various time intervals. A dish with a 1 m diameter, and a geometrical concentration factor of C = 10× was used. The samples were placed on the top of the focal point of

the dish for a certain amount of time without any cooling. The photocatalytic activity of chitosan/silicotitanate (CHMix) in concentrated sunlight is presented in Scheme 1. The photocatalytic activity assessment of chitosan silicotitanate (CHMix)in both concentrated sunlight and direct sunlight used the same procedure. As the time of highest adsorption varied with composites and dyes, the time gap and points for all samples were the same. To assess the reusability of a synthetic photocatalyst, a five-cycle reusability experiment for CR and RB degradation was conducted. The photocatalyst was recovered by centrifugation, washed with ethanol four times, and dried for 18 h at 75 °C after each cycle.

3.6. Scavenger Experiments

In order to propose a photocatalytic mechanism for CR and RB degradation, key active species such as $^{\bullet}OH$, h^+, $^{\bullet}O_2$, H_2O_2, and e^- were investigated. First, 0.5 mmol/L of methanol ($^{\bullet}OH$), isopropanol ($^{\bullet}OH$), disodium ethylene diamine tetra acetate (EDTA-2Na) (h^+), p-benzoquinone ($^{\bullet}O_2$), $AgNO_3(e^-)$, and Fe (II) (H_2O_2) were used in the scavenger experiments for reactive species detection, respectively. The CHMix heterojunction radical tests against CR and RB dye degradation were carried out under the same reaction conditions but with different scavengers.

4. Conclusions

This study described a successful development of chitosan/silicotitanate (CHMix) nanocomposite as a highly efficient photocatalyst for the degradation of organic dyes using the green synthesis technique. SEM-EDX, FT-IR, BET, and XRD were used to characterize the nanostructures' structure and morphological properties. All morphologies (chitosan, S1, S2, S3, and CHMix) demonstrated varying degradation efficiencies, with the CHMix demonstrating the highest degradation percentage. All of the catalysts developed were tested for photocatalytic decolorization of RB and CR dyes. The molar ratio of titanate loading and the solution pH had a significant impact on the degradation process. Among all chitosan/silicotitanate compound (CHMix) demonstrated the highest decolorization efficiency for both dyes and reaching 99.9% and 95.76% for RB and CR, respectively, when exposed to sunlight. Additionally, the CHMix sample has unique optical characteristics that may make it easier for it to excite, which would also result in greater photocatalytic activity. Based on degradation efficiency, CHMix can be regarded as an excellent candidate photocatalyst material for wastewater treatment.

References

1. Singh, A.; Singh, A.K.; Liu, J.; Kumar, A. Syntheses, Design Strategies, and Photocatalytic Charge Dynamics of Metal-Organic Frameworks (MOFs): A Catalyzed Photo-Degradation Approach towards Organic Dyes. *Catal. Sci. Technol.* **2021**, *11*, 3946–3989. [CrossRef]
2. Rao, C.; Zhou, L.; Pan, Y.; Lu, C.; Qin, X.; Sakiyama, H.; Muddassir, M.; Liu, J. The Extra-Large Calixarene-Based MOFs-Derived Hierarchical Composites for Photocatalysis of Dye: Facile Syntheses and Contribution of Carbon Species. *J. Alloys Compd.* **2022**, *897*, 163178. [CrossRef]

3. Qin, N.; Pan, A.; Yuan, J.; Ke, F.; Wu, X.; Zhu, J.; Liu, J.; Zhu, J. One-Step Construction of a Hollow Au@Bimetal-Organic Framework Core-Shell Catalytic Nanoreactor for Selective Alcohol Oxidation Reaction. *ACS Appl. Mater. Interfaces* **2021**, *13*, 12463–12471. [CrossRef]

4. Kumar, A.; Rana, A.; Sharma, G.; Naushad, M.; Dhiman, P.; Kumari, A.; Stadler, F.J. Recent Advances in Nano-Fenton Catalytic Degradation of Emerging Pharmaceutical Contaminants. *J. Mol. Liq.* **2019**, *290*, 111177. [CrossRef]

5. Sharma, G.; Kumar, A.; Naushad, M.; Thakur, B.; Vo, D.V.N.; Gao, B.; Al-Kahtani, A.A.; Stadler, F.J. Adsorptional-Photocatalytic Removal of Fast Sulphon Black Dye by Using Chitin-Cl-Poly(Itaconic Acid-Co-Acrylamide)/Zirconium Tungstate Nanocomposite Hydrogel. *J. Hazard. Mater.* **2021**, *416*, 125714. [CrossRef]

6. Ochoa-Gutiérrez, K.S.; Tabares-Aguilar, E.; Mueses, M.Á.; Machuca-Martínez, F.; Li Puma, G. A Novel Prototype Offset Multi Tubular Photoreactor (OMTP) for Solar Photocatalytic Degradation of Water Contaminants. *Chem. Eng. J.* **2018**, *341*, 628–638. [CrossRef]

7. Malato, S.; Maldonado, M.I.; Fernández-Ibáñez, P.; Oller, I.; Polo, I.; Sánchez-Moreno, R. Decontamination and Disinfection of Water by Solar Photocatalysis: The Pilot Plants of the Plataforma Solar de Almeria. *Mater. Sci. Semicond. Process.* **2016**, *42*, 15–23. [CrossRef]

8. Spasiano, D.; Marotta, R.; Malato, S.; Fernandez-Ibañez, P.; Di Somma, I. Solar Photocatalysis: Materials, Reactors, Some Commercial, and Pre-Industrialized Applications. A Comprehensive Approach. *Appl. Catal. B Environ.* **2015**, *170–171*, 90–123. [CrossRef]

9. Malato, S.; Blanco, J.; Vidal, A.; Alarcón, D.; Maldonado, M.I.; Cáceres, J.; Gernjak, W. Applied Studies in Solar Photocatalytic Detoxification: An Overview. *Sol. Energy* **2003**, *75*, 329–336. [CrossRef]

10. Chong, M.N.; Jin, B.; Chow, C.W.K.; Saint, C. Recent Developments in Photocatalytic Water Treatment Technology: A Review. *Water Res.* **2010**, *44*, 2997–3027. [CrossRef]

11. De la Cruz, N.; Dantas, R.F.; Giménez, J.; Esplugas, S. Photolysis and TiO_2 Photocatalysis of the Pharmaceutical Propranolol: Solar and Artificial Light. *Appl. Catal. B Environ.* **2013**, *130–131*, 249–256. [CrossRef]

12. Zhu, D.; Cai, L.; Sun, Z.; Zhang, A.; Héroux, P.; Kim, H.; Yu, W.; Liu, Y. Efficient Degradation of Tetracycline by RGO@black Titanium Dioxide Nanofluid via Enhanced Catalysis and Photothermal Conversion. *Sci. Total Environ.* **2021**, *787*, 147536. [CrossRef] [PubMed]

13. Chen, F.; Feng, H.F.; Luo, W.; Wang, P.; Yu, H.G.; Fan, J.J. Simultaneous Realization of Direct Photodeposition and High H_2-Production Activity of Amorphous Cobalt Sulfide Nanodot-Modified RGO/TiO_2 Photocatalyst. *Rare Met.* **2021**, *40*, 3125–3134. [CrossRef]

14. Chen, B.; Zhang, X.; Xia, Y.; Liu, G.; Sang, H.; Liu, Y.; Yuan, J.; Liu, J.; Ma, C.; Liang, Y.; et al. Harnessing Synchronous Photothermal and Photocatalytic Effects of Cryptomelane-Type MnO2nanowires towards Clean Water Production. *J. Mater. Chem. A* **2021**, *9*, 2414–2420. [CrossRef]

15. Chen, Y.; Xu, M.; Wen, J.; Wan, Y.; Zhao, Q.; Cao, X.; Ding, Y.; Wang, Z.L.; Li, H.; Bian, Z. Selective Recovery of Precious Metals through Photocatalysis. *Nat. Sustain.* **2021**, *4*, 618–626. [CrossRef]

16. Marimuthu, S.; Antonisamy, A.J.; Malayandi, S.; Rajendran, K.; Tsai, P.C.; Pugazhendhi, A.; Ponnusamy, V.K. Silver Nanoparticles in Dye Effluent Treatment: A Review on Synthesis, Treatment Methods, Mechanisms, Photocatalytic Degradation, Toxic Effects and Mitigation of Toxicity. *J. Photochem. Photobiol. B Biol.* **2020**, *205*, 111823. [CrossRef]

17. Zhang, Z.; Sun, J.; Chen, X.; Wu, G.; Jin, Z.; Guo, D.; Liu, L. The Synergistic Effect of Enhanced Photocatalytic Activity and Photothermal Effect of Oxygen-Deficient Ni/Reduced Graphene Oxide Nanocomposite for Rapid Disinfection under near-Infrared Irradiation. *J. Hazard. Mater.* **2021**, *419*, 126462. [CrossRef]

18. Feng, Y.; Xu, M.; Liu, H.; Li, W.; Li, H.; Bian, Z. Charge Separation and Interfacial Selectivity Induced by Synergistic Effect of Ferroelectricity and Piezoelectricity on $PbTiO_3$ Monocrystalline Nanoplates. *Nano Energy* **2020**, *73*, 104768. [CrossRef]

19. Fan, D.; Lu, Y.; Zhang, H.; Xu, H.; Lu, C.; Tang, Y.; Yang, X. Synergy of Photocatalysis and Photothermal Effect in Integrated 0D Perovskite Oxide/2D MXene Heterostructures for Simultaneous Water Purification and Solar Steam Generation. *Appl. Catal. B Environ.* **2021**, *295*, 120285. [CrossRef]

20. Cheng, Q.; Zhang, G.K. Enhanced Photocatalytic Performance of Tungsten-Based Photocatalysts for Degradation of Volatile Organic Compounds: A Review. *Tungsten* **2020**, *2*, 240–250. [CrossRef]

21. Wang, Y.; Liu, T.; Li, H.; Liu, B.; Yang, L. Tungsten-Based Photocatalysts with UV–Vis–NIR Photocatalytic Capacity: Progress and Opportunity. *Tungsten* **2019**, *1*, 247–257. [CrossRef]

22. Wang, M.; Wang, P.; Zhang, J.; Li, C.; Jin, Y. A Ternary $Pt/Au/TiO_2$-Decorated Plasmonic Wood Carbon for High-Efficiency Interfacial Solar Steam Generation and Photodegradation of Tetracycline. *ChemSusChem* **2019**, *12*, 467–472. [CrossRef] [PubMed]

23. Wang, C.; Wang, Y.; Song, X.; Huang, M.; Jiang, H. A Facile and General Strategy to Deposit Polypyrrole on Various Substrates for Efficient Solar-Driven Evaporation. *Adv. Sustain. Syst.* **2019**, *3*, 1800108. [CrossRef]

24. Wang, X.; Liu, Q.; Wu, S.; Xu, B.; Xu, H. Multilayer Polypyrrole Nanosheets with Self-Organized Surface Structures for Flexible and Efficient Solar–Thermal Energy Conversion. *Adv. Mater.* **2019**, *31*, 1807716. [CrossRef] [PubMed]

25. Zhou, H.; Xue, C.; Chang, Q.; Yang, J.; Hu, S. Assembling Carbon Dots on Vertically Aligned Acetate Fibers as Ideal Salt-Rejecting Evaporators for Solar Water Purification. *Chem. Eng. J.* **2021**, *421*, 129822. [CrossRef]

26. Liang, L.; Chang, Q.; Cai, T.; Li, N.; Xue, C.; Yang, J.; Hu, S. Combining Carbon Dots with WO_{3-x} Nanodots for Utilizing the Full Spectrum of Solar Radiation in Photocatalysis. *Chem. Eng. J.* **2022**, *428*, 131139. [CrossRef]

27. Zhou, S.; Wang, Y.; Zhou, K.; Ba, D.; Ao, Y.; Wang, P. In-Situ Construction of Z-Scheme g-C$_3$N$_4$/WO$_3$ Composite with Enhanced Visible-Light Responsive Performance for Nitenpyram Degradation. *Chin. Chem. Lett.* **2021**, *32*, 2179–2182. [CrossRef]

28. Du, C.; Yan, B.; Yang, G. Promoting Photocatalytic Hydrogen Evolution by Introducing Hot Islands: SnSe Nanoparticles on ZnIn$_2$S$_4$ Monolayer. *Chem. Eng. J.* **2021**, *404*, 126477. [CrossRef]

29. Xu, H.; She, X.; Fei, T.; Song, Y.; Liu, D.; Li, H.; Yang, X.; Yang, J.; Li, H.; Song, L.; et al. Metal-Oxide-Mediated Subtractive Manufacturing of Two-Dimensional Carbon Nitride for High-Efficiency and High-Yield Photocatalytic H$_2$ Evolution. *ACS Nano* **2019**, *13*, 11294–11302. [CrossRef]

30. Xu, Y.; Ma, J.; Han, Y.; Zhang, J.; Cui, F.; Zhao, Y.; Li, X.; Wang, W. Multifunctional CuO Nanowire Mesh for Highly Efficient Solar Evaporation and Water Purification. *ACS Sustain. Chem. Eng.* **2019**, *7*, 5476–5485. [CrossRef]

31. Naushad, M.; ALOthman, Z.A.; Sharma, G.; Inamuddin. Kinetics, Isotherm and Thermodynamic Investigations for the Adsorption of Co(II) Ion onto Crystal Violet Modified Amberlite IR-120 Resin. *Ionics* **2015**, *21*, 1453–1459. [CrossRef]

32. Haounati, R.; Ighnih, H.; Malekshah, R.E.; Alahiane, S.; Alakhras, F.; Alabbad, E.; Alghamdi, H.; Ouachtak, H.; Addi, A.A.; Jada, A. Exploring ZnO/Montmorillonite Photocatalysts for the Removal of Hazardous RhB Dye: A Combined Study Using Molecular Dynamics Simulations and Experiments. *Mater. Today Commun.* **2023**, *35*, 105915. [CrossRef]

33. Soussi, A.; Ait hssi, A.; Boulkaddat, L.; Boujnah, M.; Abouabassi, K.; Haounati, R.; Asbayou, A.; Elfanaoui, A.; Markazi, R.; Ihlal, A.; et al. First Principle Study of Electronic, Optical and Electrical Properties of Mo Doped TiO$_2$. *Comput. Condens. Matter* **2021**, *29*, e00606. [CrossRef]

34. Ding, P.; Ji, H.; Li, P.; Liu, Q.; Wu, Y.; Guo, M.; Zhou, Z.; Gao, S.; Xu, W.; Liu, W.; et al. Visible-Light Degradation of Antibiotics Catalyzed by Titania/Zirconia/Graphitic Carbon Nitride Ternary Nanocomposites: A Combined Experimental and Theoretical Study. *Appl. Catal. B Environ.* **2022**, *300*, 120633. [CrossRef]

35. Jayanthi Kalaivani, G.; Suja, S.K. TiO$_2$ (Rutile) Embedded Inulin—A Versatile Bio-Nanocomposite for Photocatalytic Degradation of Methylene Blue. *Carbohydr. Polym.* **2016**, *143*, 51–60. [CrossRef]

36. Zhu, H.; Jiang, R.; Fu, Y.; Guan, Y.; Yao, J.; Xiao, L.; Zeng, G. Effective Photocatalytic Decolorization of Methyl Orange Utilizing TiO$_2$/ZnO/Chitosan Nanocomposite Films under Simulated Solar Irradiation. *Desalination* **2012**, *286*, 41–48. [CrossRef]

37. Zhu, H.; Jiang, R.; Xiao, L.; Liu, L.; Cao, C.; Zeng, G. CdS Nanocrystals/TiO$_2$/Crosslinked Chitosan Composite: Facile Preparation, Characterization and Adsorption-Photocatalytic Properties. *Appl. Surf. Sci.* **2013**, *273*, 661–669. [CrossRef]

38. Sharma, A.; Ming, J.; Liu, N.; Sun, X.; Zhu, Y.; Yano, M.; Chen, G.; Yang, Y. Sustainable and Efficient Reduction of Pollutants by Immobilized PEG-P/Ag/Ag$_2$O/Ag$_3$PO$_4$/TiO$_2$ Photocatalyst for Purification of Saline Wastewater. *Mar. Pollut. Bull.* **2022**, *179*, 113731. [CrossRef]

39. Wu, Y.; Ji, H.; Liu, Q.; Sun, Z.; Li, P.; Ding, P.; Guo, M.; Yi, X.; Xu, W.; Wang, C.C.; et al. Visible Light Photocatalytic Degradation of Sulfanilamide Enhanced by Mo Doping of BiOBr Nanoflowers. *J. Hazard. Mater.* **2022**, *424*, 127563. [CrossRef]

40. Li, P.; Zhou, Z.; Wang, Q.; Guo, M.; Chen, S.; Low, J.; Long, R.; Liu, W.; Ding, P.; Wu, Y.; et al. Visible-Light-Driven Nitrogen Fixation Catalyzed by Bi$_5$O$_7$Br Nanostructures: Enhanced Performance by Oxygen Vacancies. *J. Am. Chem. Soc.* **2020**, *142*, 12430–12439. [CrossRef]

41. Byrne, C.; Dervin, S.; Hermosilla, D.; Merayo, N.; Blanco, Á.; Hinder, S.; Harb, M.; Dionysiou, D.D.; Pillai, S.C. Solar Light Assisted Photocatalytic Degradation of 1,4-Dioxane Using High Temperature Stable Anatase W-TiO$_2$ Nanocomposites. *Catal. Today* **2021**, *380*, 199–208. [CrossRef]

42. Fagan, R.; McCormack, D.E.; Hinder, S.; Pillai, S.C. Improved High Temperature Stability of Anatase TiO$_2$ Photocatalysts by N, F, P Co-Doping. *Mater. Des.* **2016**, *96*, 44–53. [CrossRef]

43. Kotp, Y.H. Fabrication of Cerium Titanate Cellulose Fiber Nanocomposite Materials for the Removal of Methyl Orange and Methylene Blue from Polluted Water by Photocatalytic Degradation. *Environ. Sci. Pollut. Res.* **2022**, *29*, 81583–81608. [CrossRef] [PubMed]

44. Papp, S.; Kõrösi, L.; Meynen, V.; Cool, P.; Vansant, E.F.; Dékány, I. The Influence of Temperature on the Structural Behaviour of Sodium Tri- and Hexa-Titanates and Their Protonated Forms. *J. Solid State Chem.* **2005**, *178*, 1614–1619. [CrossRef]

45. Ramírez-Salgado, J.; Djurado, E.; Fabry, P. Synthesis of Sodium Titanate Composites by Sol-Gel Method for Use in Gas Potentiometric Sensors. *J. Eur. Ceram. Soc.* **2004**, *24*, 2477–2483. [CrossRef]

46. Feng, M.; You, W.; Wu, Z.; Chen, Q.; Zhan, H. Mildly Alkaline Preparation and Methylene Blue Adsorption Capacity of Hierarchical Flower-like Sodium Titanate. *ACS Appl. Mater. Interfaces* **2013**, *5*, 12654–12662. [CrossRef] [PubMed]

47. Gadore, V.; Mishra, S.R.; Ahmaruzzaman, M. Green and Environmentally Sustainable Fabrication of SnS$_2$ Quantum Dots/Chitosan Nanocomposite for Enhanced Photocatalytic Performance: Effect of Process Variables, and Water Matrices. *J. Hazard. Mater.* **2022**, *444*, 130301. [CrossRef] [PubMed]

48. Zhang, M.; Yuan, R.; Chai, Y.; Li, W.; Zhong, H.; Wang, C. Glucose Biosensor Based on Titanium Dioxide-Multiwall Carbon Nanotubes-Chitosan Composite and Functionalized Gold Nanoparticles. *Bioprocess Biosyst. Eng.* **2011**, *34*, 1143–1150. [CrossRef]

49. Alexandre, M.; Dubois, P. Polymer-Layered Silicate Nanocomposites: Preparation, Properties and Uses of a New Class of Materials. *Mater. Sci. Eng. R Rep.* **2000**, *28*, 1–63. [CrossRef]

50. Zhou, Z.; Peng, X.; Zhong, L.; Wu, L.; Cao, X.; Sun, R.C. Electrospun Cellulose Acetate Supported Ag@AgCl Composites with Facet-Dependent Photocatalytic Properties on Degradation of Organic Dyes under Visible-Light Irradiation. *Carbohydr. Polym.* **2016**, *136*, 322–328. [CrossRef]

51. Habiba, U.; Islam, M.S.; Siddique, T.A.; Afifi, A.M.; Ang, B.C. Adsorption and Photocatalytic Degradation of Anionic Dyes on Chitosan/PVA/Na-Titanate/TiO$_2$ Composites Synthesized by Solution Casting Method. *Carbohydr. Polym.* **2016**, *149*, 317–331. [CrossRef]

52. Martinová, L.; Lubasová, D. Electrospun Chitosan Based Nanofibers. *Res. J. Text. Appar.* **2008**, *12*, 72–79. [CrossRef]

53. Wan Ngah, W.S.; Teong, L.C.; Hanafiah, M.A.K.M. Adsorption of Dyes and Heavy Metal Ions by Chitosan Composites: A Review. *Carbohydr. Polym.* **2011**, *83*, 1446–1456. [CrossRef]

54. Qin, L.; Li, Y.; Liang, F.; Li, L.; Lan, Y.; Li, Z.; Lu, X.; Yang, M.; Ma, D. A Microporous 2D Cobalt-Based MOF with Pyridyl Sites and Open Metal Sites for Selective Adsorption of CO$_2$. *Microporous Mesoporous Mater.* **2022**, *341*, 112098. [CrossRef]

55. Qin, L.; Liang, F.; Li, Y.; Wu, J.; Guan, S.; Wu, M.; Xie, S.; Luo, M.; Ma, D. A 2D Porous Zinc-Organic Framework Platform for Loading of 5-Fluorouracil. *Inorganics* **2022**, *10*, 202. [CrossRef]

56. Nyman, M.; Gu, B.X.; Wang, L.M.; Ewing, R.C.; Nenoff, T.M. Synthesis and Characterization of a New Microporous Cesium Silicotitanate (SNL-B) Molecular Sieve. *Microporous Mesoporous Mater.* **2000**, *40*, 115–125. [CrossRef]

57. Eissa, D.; Hegab, R.H.; Abou-Shady, A.; Kotp, Y.H. Green Synthesis of ZnO, MgO and SiO$_2$ Nanoparticles and Its Effect on Irrigation Water, Soil Properties, and Origanum Majorana Productivity. *Sci. Rep.* **2022**, *12*, 5780. [CrossRef]

58. Nyman, M.; Nenoff, T.; Headley, T. *Characterization of UOP IONSIV® IE-911*; Sandia National Labs: Albuquerque, NM, USA, 2001.

59. Poojary, D.M.; Cahill, R.A.; Clearfield, A. Synthesis, Crystal Structures, and Ion-Exchange Properties of a Novel Porous Titanosilicate. *Chem. Mater.* **1994**, *6*, 2364–2368. [CrossRef]

60. Yaseen, R.; Kotp, Y.H.; Eissa, D. The Impact of Production of Silver Nanoparticles Using Soil Fungi and Its Applications for Reducing Irrigation Water Salinity. *J. Water Land Dev.* **2020**, *46*, 216–228. [CrossRef]

61. Hagab, R.H.; Kotp, Y.H.; Eissa, D. Using Nanotechnology for Enhancing Phosphorus Fertilizer Use Efficiency of Peanut Bean Grown in Sandy Soils. *J. Adv. Pharm. Educ. Res.* **2018**, *8*, 59–67.

62. Ebisike, K.; Okoronkwo, A.E.; Alaneme, K.K. Synthesis and Characterization of Chitosan–Silica Hybrid Aerogel Using Sol-Gel Method. *J. King Saud Univ. Sci.* **2020**, *32*, 550–554. [CrossRef]

63. Wang, R.; Luo, Z.; Tan, Q.; Wang, R.; Chen, S.; Shu, J.; Chen, M.; Xiao, Z. Sol-Gel Hydrothermal Synthesis of Nano Crystalline Silicotitanate and Its Strontium and Cesium Adsorption. *Environ. Sci. Pollut. Res.* **2020**, *27*, 4404–4413. [CrossRef]

64. Kumirska, J.; Czerwicka, M.; Kaczyński, Z.; Bychowska, A.; Brzozowski, K.; Thöming, J.; Stepnowski, P. Application of Spectroscopic Methods for Structural Analysis of Chitin and Chitosan. *Mar. Drugs* **2010**, *8*, 1567–1636. [CrossRef] [PubMed]

65. Ramya, R.; Sudha, P.; Mahalakshmi, D. Preparation and Characterization of Chitosan Binary Blend. *Int. J. Sci. Res. Publ.* **2012**, *2*, 1–9.

66. Uda, M.N.A.; Gopinath, S.C.B.; Hashim, U.; Halim, N.H.; Parmin, N.A.; Afnan Uda, M.N.; Anbu, P. Production and Characterization of Silica Nanoparticles from Fly Ash: Conversion of Agro-Waste into Resource. *Prep. Biochem. Biotechnol.* **2021**, *51*, 86–95. [CrossRef] [PubMed]

67. Ramanery, F.P.; Mansur, A.A.P.; Mansur, H.S. One-Step Colloidal Synthesis of Biocompatible Water-Soluble ZnS Quantum Dot/Chitosan Nanoconjugates. *Nanoscale Res. Lett.* **2013**, *8*, 512. [CrossRef] [PubMed]

68. Luk, C.J.; Yip, J.; Yuen, C.M.; Kan, C.; Lam, K. A Comprehensive Study on Adsorption Behaviour of Direct, Reactive and Acid Dyes on Crosslinked and Non-Crosslinked Chitosan Beads. *J. Fiber Bioeng. Inform.* **2014**, *7*, 35–52. [CrossRef]

69. Al-Shemy, M.T.; Al-Sayed, A.; Dacrory, S. Fabrication of Sodium Alginate/Graphene Oxide/Nanocrystalline Cellulose Scaffold for Methylene Blue Adsorption: Kinetics and Thermodynamics Study. *Sep. Purif. Technol.* **2022**, *290*, 120825. [CrossRef]

70. Thommes, K.M.; Kaneko, A.V.; Neimark, J.P.; Olivier, F.; Rodriguez-Reinoso, J.; Rouquerol, K.S.S. Physisorption of Gases, with Special Reference to the Evaluation of Surface Area and Pore Size Distribution. *Chem. Int. Newsmag. IUPAC* **2014**, *33*. [CrossRef]

71. He, X.; Gan, J.; Fakhri, A.; Dizaji, B.F.; Azarbaijan, M.H.; Hosseini, M. Preparation of Ceric Oxide and Cobalt Sulfide-Ceric Oxide/Cellulose-Chitosan Nanocomposites as a Novel Catalyst for Efficient Photocatalysis and Antimicrobial Study. *Int. J. Biol. Macromol.* **2020**, *143*, 952–957. [CrossRef]

72. Jabbar, Z.H.; Graimed, B.H.; Issa, M.A.; Ammar, S.H.; Ebrahim, S.E.; Khadim, H.J.; Okab, A.A. Photocatalytic Degradation of Congo Red Dye Using Magnetic Silica-Coated Ag$_2$WO$_4$/Ag$_2$S as Type I Heterojunction Photocatalyst: Stability and Mechanisms Studies. *Mater. Sci. Semicond. Process.* **2023**, *153*, 107151. [CrossRef]

73. Makuła, P.; Pacia, M.; Macyk, W. How To Correctly Determine the Band Gap Energy of Modified Semiconductor Photocatalysts Based on UV-Vis Spectra. *J. Phys. Chem. Lett.* **2018**, *9*, 6814–6817. [CrossRef] [PubMed]

74. Toro, R.G.; Adel, A.M.; de Caro, T.; Brunetti, B.; Al-Shemy, M.T.; Caschera, D. A Facile One-Pot Approach to the Fabrication of Nanocellulose–Titanium Dioxide Nanocomposites with Promising Photocatalytic and Antimicrobial Activity. *Materials* **2022**, *15*, 5789. [CrossRef] [PubMed]

75. Kandil, H.; Ali, H. Simultaneous Removal of Cationic Crystal Violet and Anionic Reactive Yellow Dyes Using Eco-Friendly Chitosan Functionalized by Talc and Cloisite 30B. *J. Polym. Environ.* **2022**, *31*, 1456–1477. [CrossRef]

76. Cao, C.; Xiao, L.; Liu, L.; Zhu, H.; Chen, C.; Gao, L. Visible-Light Photocatalytic Decolorization of Reactive Brilliant Red X-3B on Cu$_2$O/Crosslinked-Chitosan Nanocomposites Prepared via One Step Process. *Appl. Surf. Sci.* **2013**, *271*, 105–112. [CrossRef]

77. Zhu, J.; Gao, Q. Microporous and Mesoporous Materials Mesoporous MCo$_2$O$_4$ (M = Cu, Mn and Ni) Spinels: Structural Replication, Characterization and Catalytic Application in CO Oxidation. *Microporous Mesoporous Mater.* **2009**, *124*, 144–152. [CrossRef]

78. Hasmath Farzana, M.; Meenakshi, S. Synergistic Effect of Chitosan and Titanium Dioxide on the Removal of Toxic Dyes by the Photodegradation Technique. *Ind. Eng. Chem. Res.* **2014**, *53*, 55–63. [CrossRef]

79. Mohamed, M.A.; Salleh, W.N.W.; Jaafar, J.; Ismail, A.F.; Nor, N.A.M. Photodegradation of Phenol by N-Doped TiO_2 Anatase/Rutile Nanorods Assembled Microsphere under UV and Visible Light Irradiation. *Mater. Chem. Phys.* **2015**, *162*, 113–123. [CrossRef]

80. Su, X.; Liao, Q.; Liu, L.; Meng, R.; Qian, Z.; Gao, H.; Yao, J. Cu_2O Nanoparticle-Functionalized Cellulose-Based Aerogel as High-Performance Visible-Light Photocatalyst. *Cellulose* **2017**, *24*, 1017–1029. [CrossRef]

81. Harraz, F.A.; Mohamed, R.M.; Rashad, M.M.; Wang, Y.C.; Sigmund, W. Magnetic Nanocomposite Based on Titania-Silica/Cobalt Ferrite for Photocatalytic Degradation of Methylene Blue Dye. *Ceram. Int.* **2014**, *40*, 375–384. [CrossRef]

82. Vieira, G.B.; José, H.J.; Peterson, M.; Baldissarelli, V.Z.; Alvarez, P.; de Fátima Peralta Muniz Moreira, R. CeO_2/TiO_2 Nanostructures Enhance Adsorption and Photocatalytic Degradation of Organic Compounds in Aqueous Suspension. *J. Photochem. Photobiol. A Chem.* **2018**, *353*, 325–336. [CrossRef]

83. Chiou, C.H.; Wu, C.Y.; Juang, R.S. Influence of Operating Parameters on Photocatalytic Degradation of Phenol in UV/TiO_2 Process. *Chem. Eng. J.* **2008**, *139*, 322–329. [CrossRef]

84. Yu, J.; Wang, K.; Xiao, W.; Cheng, B. Photocatalytic Reduction of CO_2 into Hydrocarbon Solar Fuels over G-C_3N_4-Pt Nanocomposite Photocatalysts. *Phys. Chem. Chem. Phys.* **2014**, *16*, 11492–11501. [CrossRef]

85. Barakat, M.A.; Tseng, J.M.; Huang, C.P. Hydrogen Peroxide-Assisted Photocatalytic Oxidation of Phenolic Compounds. *Appl. Catal. B Environ.* **2005**, *59*, 99–104. [CrossRef]

86. Yang, Y.; Ali, N.; Khan, A.; Khan, S.; Khan, S.; Khan, H.; Xiaoqi, S.; Ahmad, W.; Uddin, S.; Ali, N.; et al. Chitosan-Capped Ternary Metal Selenide Nanocatalysts for Efficient Degradation of Congo Red Dye in Sunlight Irradiation. *Int. J. Biol. Macromol.* **2021**, *167*, 169–181. [CrossRef] [PubMed]

87. Suich, R.; Derringer, G. Simultaneous Optimization of Several Response Variables. *J. Qual. Technol.* **1980**, *12*, 214–219.

88. Velmurugan, S.; Balu, S.; Palanisamy, S.; Yang, T.C.K.; Velusamy, V.; Chen, S.W.; El-Shafey, E.S.I. Synthesis of Novel and Environmental Sustainable AgI-Ag_2S Nanospheres Impregnated g-C_3N_4 Photocatalyst for Efficient Degradation of Aqueous Pollutants. *Appl. Surf. Sci.* **2020**, *500*, 143991. [CrossRef]

89. Mandal, S.; Adhikari, S.; Pu, S.; Wang, X.; Kim, D.H.; Patel, R.K. Interactive Fe_2O_3/Porous SiO_2 Nanospheres for Photocatalytic Degradation of Organic Pollutants: Kinetic and Mechanistic Approach. *Chemosphere* **2019**, *234*, 596–607. [CrossRef] [PubMed]

90. Durán, A.; Monteagudo, J.M. Solar Photocatalytic Degradation of Reactive Blue 4 Using a Fresnel Lens. *Water Res.* **2007**, *41*, 690–698. [CrossRef]

91. Al-Obaidy, A.H.; Al-Anbari, R.H.; Mohammed, E.A. Solar Photocatalytic of Reactive Blue Dye in Aqueous Suspension of V_2O_5. *Eng. Technol. J.* **2017**, *35*, 1–8. [CrossRef]

92. Joy, M.; Nair, B.N.; Mohamed, A.A.P.; Warrier, K.G.; Hareesh, U.N.S. One-Pot Hydrothermal Synthesis of Visible-Light-Responsive MoS_2/g-CNO Heterostructures for Organic-Pollutant Degradation. *Eur. J. Inorg. Chem.* **2016**, *2016*, 3912–3920. [CrossRef]

93. He, J.; Cheng, Y.; Wang, T.; Feng, D.; Zheng, L.; Shao, D.; Wang, W.; Wang, W.; Lu, F.; Dong, H.; et al. Enhanced Photocatalytic Performances and Magnetic Recovery Capacity of Visible-Light-Driven Z-Scheme $ZnFe_2O_4$/AgBr/Ag Photocatalyst. *Appl. Surf. Sci.* **2018**, *440*, 99–106. [CrossRef]

94. Dahash, M.S.H.; Ammar, S.H.; Abdulnabi, W.A. Synthesis of Magnetic Zincoxysulfide Core/Shell Nanocomposites ($Ni@ZnO_{0.6}S_{0.4}$) for COD Photocatalytic Degradation in Oil Refinery Wastewater. *IOP Conf. Ser. Mater. Sci. Eng.* **2020**, *928*, 022063. [CrossRef]